14 February 2005

MICE scintillating-fibre tracker

First progress report

A. Khan, P. Kyberd,
Brunel

L. Tong
Edinburgh

A. Bross, J. Krider, R. Rucinski, P. Rubinov
FNAL

D. Kaplan, Y. Torun
Illinois Institute of Technology

G. Barber, M. Ellis, R. Hare, R. Goncalo†, K. Long, E. McKigney‡, C. Rogers
Imperial College London

K. Yoshimura
KEK

P. Cooke, R. Gamet
Liverpool

Y. Kuno, H. Sakamoto, A. Sato, M. Yoshida
Osaka

G. Hanson, A. Klier,
Riverside

X. Yang
UCLA

Abstract

The design of the scintillating-fibre tracker for the international Muon Ionisation Cooling Experiment (MICE) is reviewed. The first prototype of the MICE tracker was constructed over the summer of 2003. This report presents the design and construction of the prototype and the commissioning of the device in the DØ VLPC test stand at Fermilab. The active element of the tracker is constructed from 350 μm diameter scintillating fibre. The measured light yield in the prototype was 10.6 ± 0.2 photo-electrons and the measured resolution and efficiency met the specification. Results of the full tracking system proposed for MICE are presented and demonstrate that the system is capable of measuring the relative change in emittance with a precision of 1%.

---

† Now at Royal Holloway College, University of London

‡ Now at Los Alamos National Laboratory, Arizona, USA.

1. Introduction

Muon storage rings have been proposed for use as sources of intense high-energy neutrino beams and as the basis for multi-TeV lepton-antilepton colliding beam facilities [1]. Optimisation of the performance of such facilities is likely to require the phase-space compression (cooling) of the muon beam prior to acceleration and storage. The short muon-lifetime makes it impossible to employ traditional techniques to cool the beam while maintaining the muon-beam intensity. Ionisation cooling, a process in which the muon beam is passed through a series of liquid-hydrogen absorbers followed by accelerating cavities, is the technique proposed to cool the muon beam. The international Muon Ionisation Cooling Experiment (MICE) collaboration has been formed to carry out a muon-cooling demonstration experiment and its proposal to Rutherford Appleton Laboratory [2] has been approved.

The principle components of MICE are shown in figure 1 [3]. The cooling section is composed of three liquid hydrogen vessels, two sets of four 201.25 MHz accelerating cavities and a series of superconducting solenoids to transport the muon beam through the channel. The spectrometer sections upstream and downstream of the cooling channel are each composed of a superconducting solenoid instrumented with a charged-particle tracking device. MICE is conceived as a single-particle experiment in which the parameters of each muon are measured as it enters the apparatus and again as it leaves. The MICE specification requires that the relative change in emittance of approximately 10% be measured with a precision of 1%. The baseline solution for the spectrometer instrumentation in MICE uses five scintillating-fibre stations. Each station is composed of three planar layers of scintillating fibre laid out in a '*u, v, w'* arrangement. To reduce multiple Coulomb scattering of muons to an acceptable level a fibre diameter of 350 μm is required. The scintillation light is read out via 1.05 mm clear fibre light-guides. To reduce the cost of the readout electronics seven 350 μm fibres are read out through each clear-fibre light-guide.

For the proposed scintillating fibre tracker to meet the requirements imposed by MICE it is essential to demonstrate [4]:

- Through the construction, commissioning and operation of a full-scale prototype, that the light yield, cross talk, dead channel rate and degree of RF pickup are consistent with efficient, reliable operation in MICE;
- Through simulation, that the performance of the pattern recognition and track reconstruction in the presence of conservatively-estimated levels of simulated background is consistent with the measurement of a relative change in emittance with a precision of 1%.

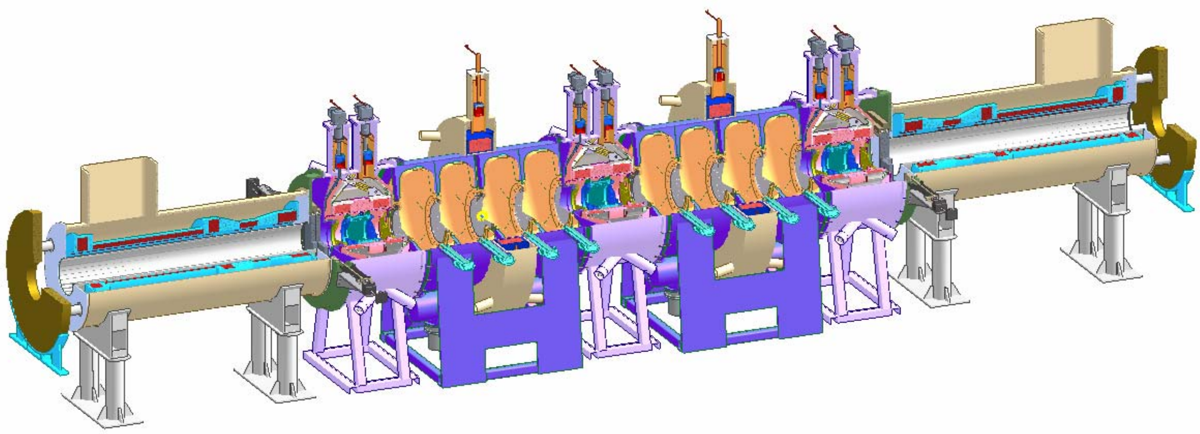

Figure 1: Drawing of the MICE experiment showing the upstream and downstream spectrometers and the MICE cooling channel.

This paper is organised as follows: a brief overview of the scintillating-fibre tracker proposed for MICE is presented in section 2; section 3 contains a detailed description of the first prototype, the optical readout and the set up in the DØ cosmic ray test stand; section 4 reports on the measurement of the intrinsic properties of the fibre to be used in the tracker; the response of the electronics to RF noise is summarised in section 5; the measurements made using the prototype in the DØ cosmic-ray test stand are described in section 6; the simulation of the full MICE tracker is described in section 7; section 8 describes the safety aspects of the system; and section 9 summarises the MICE tracker cost and schedule.

2. The MICE scintillating-fibre tracker

A schematic drawing of the scintillating-fibre tracker proposed for MICE is shown in figure 2. The super-conducting solenoid will produce an axial field of 4 T that is uniform at the 1% level over a 1.05 m region. The warm inner bore of the magnet will be 40 cm in diameter. The active area of the tracker is required to be 30 cm in diameter. The five stations that make up a tracker will be held in position by a carbon-fibre frame that will be supported at each end from the surface of the magnet cryostat. To reduce multiple Coulomb scattering, the inner bore of the solenoid will be evacuated.

The stations will be constructed using carbon fibre to give a rigid structure onto which the three "doublet"-layers of 350 μm scintillating-fibre will be glued. Each station body will be constructed from a single carbon-fibre structure that allows for the mounting of optical connectors on a flat annulus separated by a conical section from a thin, flat ring onto which the scintillating-fibre planes can be bonded. (For the prototype, the station bodies were fabricated from three carbon-fibre pieces as described in section 3.1). The read-out of the scintillation light is via clear-fibre light guides. The optical connectors on the station will mate seven 350 μm scintillating fibres to each 1.05 mm clear-fibre light guide. The light guides will transport the scintillation light from the stations to an optical patch panel that will be mounted on the end flange of the magnet cryostat. Since the tracker will be operated in a vacuum, the patch panel is required to form a vacuum seal to the cryostat end flange.

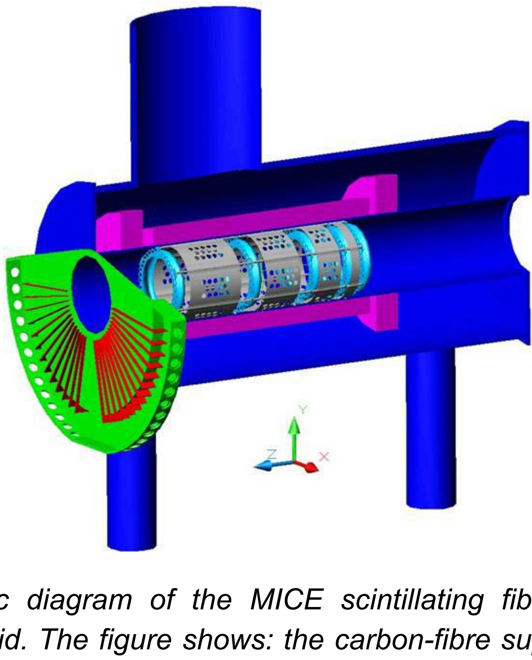

Figure 2: Schematic diagram of the MICE scintillating fibre tracker inside the spectrometer solenoid. The figure shows: the carbon-fibre support structure (grey); the carbon-fibre station bodies (light blue); the optical patch panel (green); and supports for the clear-fibre bundles (red). The walls of the magnet cryostat are shown (dark blue) and the position of the coils within the cryostat itself are also indicated (magenta). Note that, for clarity, the scintillating-fibre planes are not shown.

Three planes of scintillating fibre will be mounted on each station. Each plane will be composed of a doublet layer of scintillating fibre. In order that there be no dead spaces, the fibre layers will be offset as shown in figure 3a. The three planes will be mounted on the carbon-fibre support such that the angle between the fibres in one plane and those in another plane in the same station is 120º as shown in figure 3b.

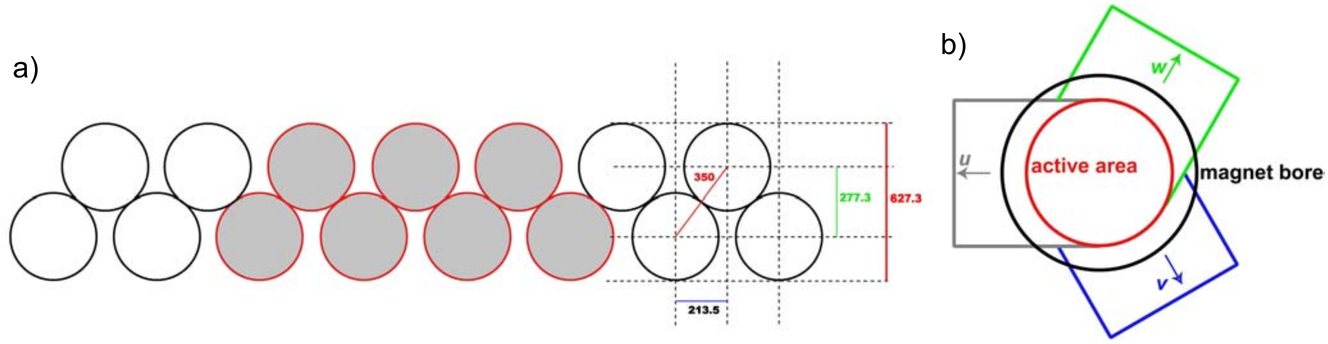

Figure 3: Detail of arrangement of fibres in a station. (a) Cross-sectional view of fibre doublet. The dimensions of the fibre and fibre spacing are indicated in μm. The fibres shown shaded indicate the seven fibres ganged for readout via a single clear fibre. (b) Layout of doublet layers in a station. The angle between the fibres in the doublet layers is 120º.

The scintillation light will be detected using Visible Light Photon Counters (VLPCs) [5]. These devices are low band-gap silicon avalanche devices that are operated at ~9 K. The VLPCs have a high quantum efficiency (~80%) and a high gain (~50 000). The light will be transported from the optical patch panel to the VLPCs using a further length of 1.05 mm clear fibre. The VLPCs will be read out using the Analogue Front End (AFE II) board being developed by the DØ collaboration [6].

3. The first MICE tracker prototype

The first prototype of the tracker proposed for the MICE experiment is shown schematically in figure 4. Three stations were fabricated, supported on carbon-fibre rods and installed inside an aluminium light box. The central station (station B) was equipped with three fibre-doublet layers as described in section 3.3. Stations A and C were each equipped with two fibre-doublet layers. This allowed the properties of station B to be studied in an unbiased manner using reconstructed cosmic-ray tracks. The distance between the stations is indicated in figure 4.

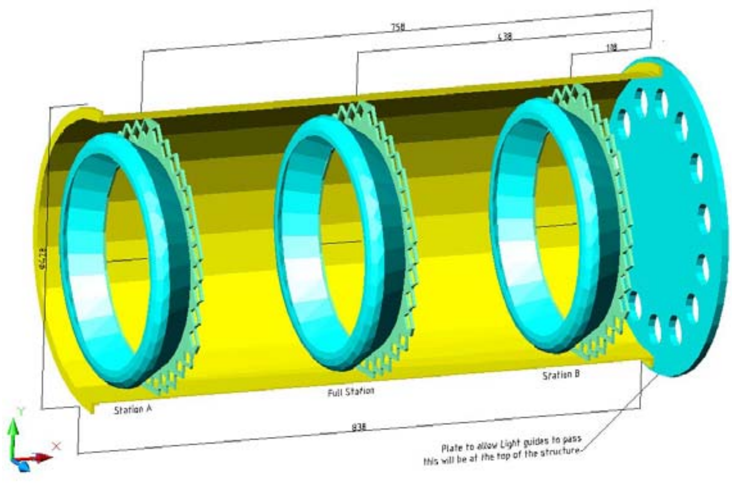

Figure 4: Schematic drawing prototype tracker showing the station bodies, the end flange and the support tube.

The scintillating fibres used in the prototype are 350 μm diameter Kuraray multi-clad doped polystyrene fibres. The primary dopant was p-terphenyl at a concentration of 1% (by weight). The secondary fluor used was 3-hydroxflavone (3HF). Fibre containing either 2500, 3500, or 5000 parts per million 3HF was used in the prototype (see table 1). For the prototype, the arrangement of fibres in a doublet layer was as indicated in figure 3a but the fibre pitch (i.e. the distance between the centres of two neighbouring fibres in the same singlet layer) was 420 μm. There were 1475 fibres in one doublet layer.

3.1 Station body fabrication

An exploded diagram of the carbon-fibre pieces which make up the station body is shown in figure 5a. Each station body was fabricated from three separate pieces of cured carbon fibre: the support/connector flange; the spacer cone; and the scintillating-fibre support. A female tool was made from aluminium, forming the shape required of the doublet-layer support. The tool was polished and had a tool release solution applied. Three layers of carbon fibre (cut to a pattern) were then applied. The assembly was vacuum-bagged and cured in an oven. The finished thickness of the scintillating-fibre support was approximately 0.8 mm. A male tool was produced from aluminium forming the shape of the large shortened cone (the spacer cone), required to connect the support/connector flange to the scintillating fibre support. The tool was treated and carbon fibre applied and cured as above. The finished thickness of the spacer cone was approximately 0.8 mm. The support/connector flange was made by applying carbon fibre directly onto a polished flat plate to a thickness of 2.4 mm. The cured plate was mounted on a CNC machine and the outer and inner profile, apertures for the optical connectors and screw holes were machined. The three separate components were then held together in a fixture and bonded using Araldite 2011.

a) b)

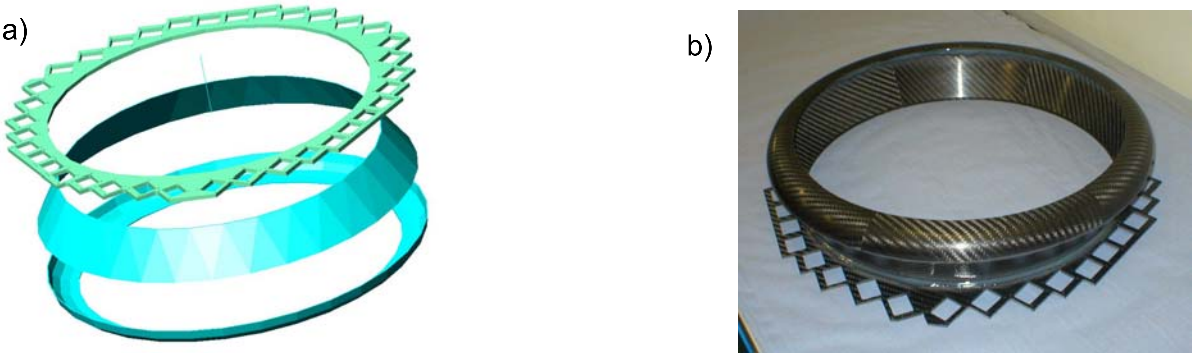

Figure 5: a) Exploded view of prototype station; b) photograph of a completed station body.

3.2 Fibre-doublet layer fabrication

All fibres were cut to length and polished on one end to allow an aluminium mirror to be applied by vapour deposition. The quality of the mirrors on the fibres used in this test was not measured. However, an average reflectivity of approximately 90% was achieved when the same technique was used for the preparation of fibre for the DØ fibre tracker [7].

The ribbons were made following the technique developed for the DØ fibre tracker. A grooved, plastic (delrin) mould was first fabricated (see figure 6a). The mould was measured on a coordinate measuring machine and the mean groove pitch was determined to be 419 μm which compares well with the target groove-pitch of 420 micron. A teflon release film (25 μm thick) was pressed into the mould with the aid of vacuum (pump-out holes were drilled into the grooves in the mould). A circular stop, fabricated from a plastic sheet, was placed over the mould to form a ribbon with the proper circular active aperture (a diameter of 31 cm). A photograph of a completed ribbon is shown in figure 6b. A tack adhesive was sprayed onto the teflon and the first layer of fibres was placed in the mould. After the first layer of fibre was in the mould the spray adhesive was applied to the fibre and the second layer of fibre (forming the doublet) was placed on top of the first. A polyurethane adhesive was spread over the fibres and a 25 μm thick mylar film was glued to the upper layer of fibre. The assembly was then clamped under pressure and the adhesive allowed to cure overnight. The resultant doublet layer was removed from the mould with the release film still attached. Finally, the release film was carefully removed from the ribbon.

a)

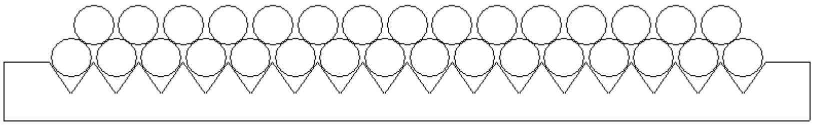

b)

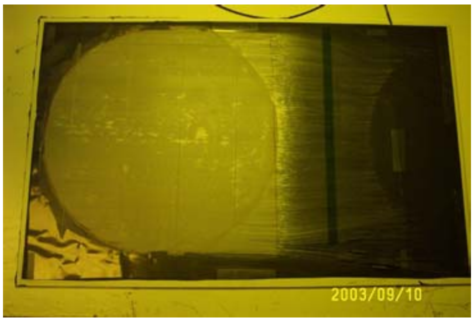

Figure 6: a) Schematic drawing of the fibre-doublet layer laid in the delrin mould. b) Photograph of a completed fibre-doublet layer.

3.3 Mounting of scintillating-fibre doublet layers on station body

The final steps in the station-fabrication procedure were:

i. *Fibre bundling*: Working from one side of the doublet layer, groups of seven neighbouring fibres were collected together and threaded into a short piece of narrow rubber tubing (see figure 7). The tubing served to keep the fibre bundles intact during the subsequent steps in the fabrication procedure and, eventually, were used to provide strain relief when the fibres were potted into the optical connector;

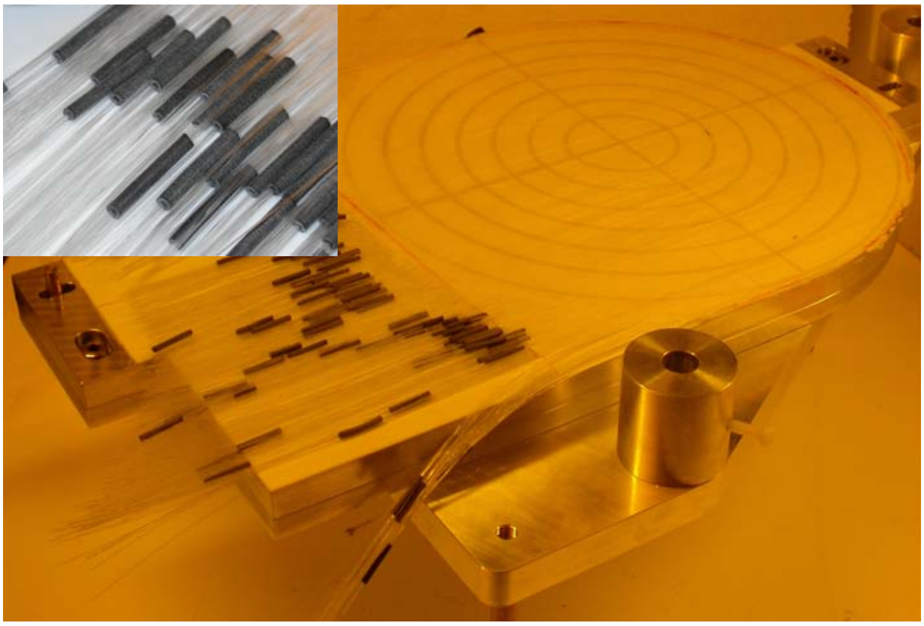

Figure 7: Fibre-doublet layer after bundling. The fibre-doublet is shown mounted on the vacuum chuck. The inset shows a detail of the rubber sleeves fitted around bundles of seven scintillating fibres.

ii. *Doublet layer – station body bonding*: The doublet layer was held on a custom made vacuum chuck. The vacuum chuck was mounted on a precision jig, the position of which could be accurately adjusted using eccentric cams. The jig-chuck assembly was mounted on a precision stage and viewed through a microscope so that the vacuum chuck, and therefore the fibres in the doublet layer, could be aligned with respect to the axis of the jig. The precision with which the fibre axis was aligned with respect to the jig axis was significantly smaller than the fibre diameter.

a) b)

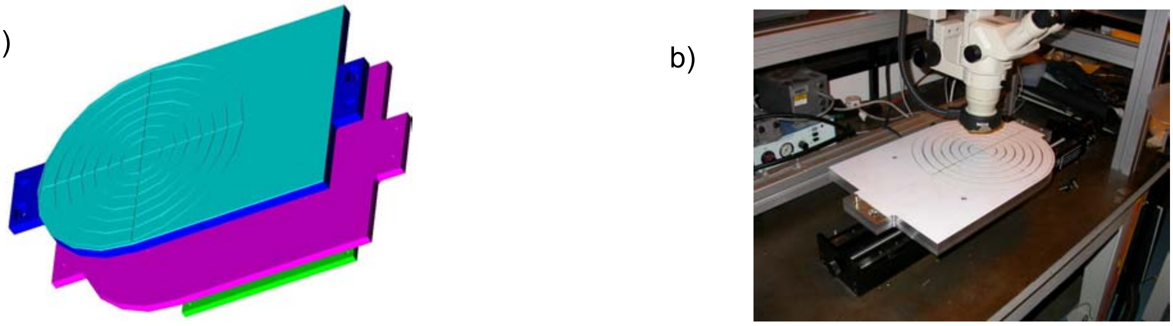

Figure 8: a) exploded diagram of the chuck. The top surface of the chuck (light blue) is machined from PTFE which is glued to an aluminium plate (dark blue). The aluminium plate is mounted using asymmetric cams to an aluminium support plate (purple). Finally, the assembly is mounted on an aluminium plate which is attached to a precision stage. b) Photograph of vacuum-chuck assembly mounted on the precision stage.

iii. *Bonding the doublet layers to the station body*: With the station body held in a custom clamp (see figure 9a), the jig-vacuum-chuck assembly was lowered onto the station body. The jig was equipped with three precision dowels that were positioned at the corners of an equilateral triangle. The clamp holding the station body was equipped with three holes which precisely matched the dowels on the jig. The jig could therefore be lowered onto the stage in one of three orientations, the angle between these orientations being 120º.

Before the first doublet layer was lowered, Araldite 2026 was applied to the station body. Subsequently, adhesive was applied to the doublet layer and the next layer lowered on top. Care was taken to ensure that a full ring of adhesive was not applied so that air could escape as the next layer was lowered onto those already present. This ensured that the scintillating-fibre planes were flat. The order in which the doublet layers were bonded to the station body is listed in table 1.

iv. *Connecterisation*: Starting with the bundle of seven fibres in the centre of a doublet layer, the bundles were passed through the appropriate hole in the MICE optical connector (see section 3.4). When a connector was fully populated, a piece of tape was placed around the fibre protruding from the back of the connector. When all connectors on a particular station had been threaded, the connectors were located in the connector flange. The pieces of rubber tubing that had served to keep the bundles together during the manufacturing process were then positioned inside the recessed area of the connector and Araldite 2026 run into the recess. A vacuum cup was positioned over the side of the connector from which the waste fibre protruded. Suction was applied until Araldite was seen to flow from the holes. A photograph of one of the stations at this point in the manufacturing process is shown in figure 9b. The glue was allowed to cure overnight. The station was then inverted so that the waste fibre protruded vertically upward. Araldite 2026 was then applied to the top surface to a depth of 2 – 3 mm. When the glue was hard the waste fibre was trimmed. Finally, the excess Araldite was removed and the connector surface polished using a diamond fly cutter. A photograph of the surface of a finished connector is shown in figure 10c.

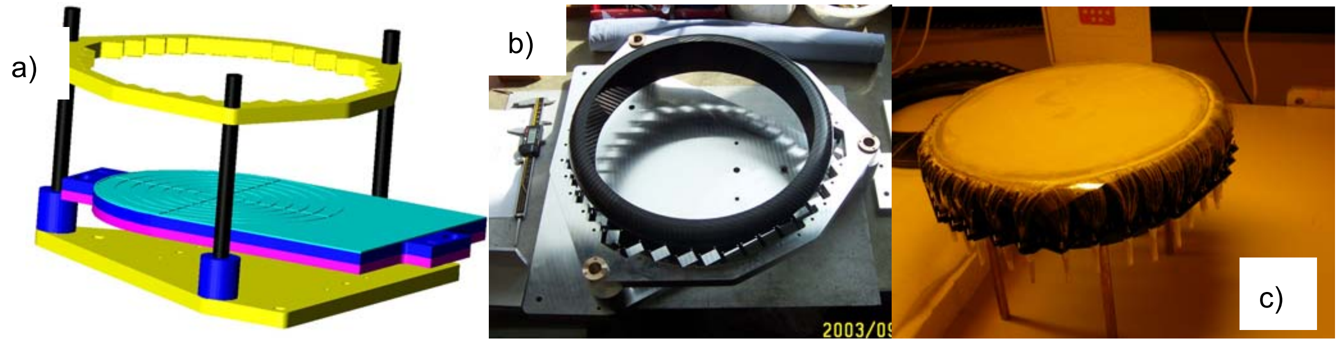

Figure 9: a) Exploded diagram showing station-body clamp and lowering jig The station-body clamp was machined from aluminium while the precision dowels and precision locating pieces were steel. b) Photograph of station body in custom clamp. c) Photograph of completed station with all three scintillating-fibre doublet layers bonded to it. The optical connectors have been fitted and potted. The photograph was taken before the excess fibre was removed from the optical connector and the connector surface polished.

Several concentrations of 3HF, the secondary dopant, were used in the fabrication of the doublet layers. Table 1 summarises the concentrations in the various stations of the prototype and lists the fibres read-out in the cosmic ray data taking.

Station	**View**	**Fibre numbers read out**	**3HF concentration (%)**
A	*V*	372 – 1247	0.50
	X	246 – 1121	0.50
B	*V*	239 – 1247	0.25
	X	323 – 1184	0.50
	W	267 – 1331	0.35
C	*X*	372 – 1247	Three sections: 0.25; 0.35; 0.50
	W	246 – 1121	0.50

Table 1: Details of the fibre doping used in the various stations and the fibres read-out in the cosmic ray data taking. Each doublet layer forms a view. The view refers to the direction in which the fibres in the doublet layer were aligned (see figure 3b). The fibre number refers to the position of the fibre in the doublet layer. With the station body resting on the connector/support flange, viewed from above with the fibres running from the rounded end of the doublet layer at the back to the optical connectors at the front, fibre number 1 is the left-most fibre.

3.4 Prototype MICE optical connector

The optical connector to be used on the station is required to mate seven 350 μm scintillating fibres to one 1.05 mm clear fibre. The prototype connector design is shown in figure 10a and a photograph of the connector in figure 10b. Eighteen 1.05 mm holes laid out in a regular pattern were drilled to take the fibres. The hole diameter was matched to the seven scintillating fibres as shown in figure 10c. The connector was machined in delrin on a CNC machine.

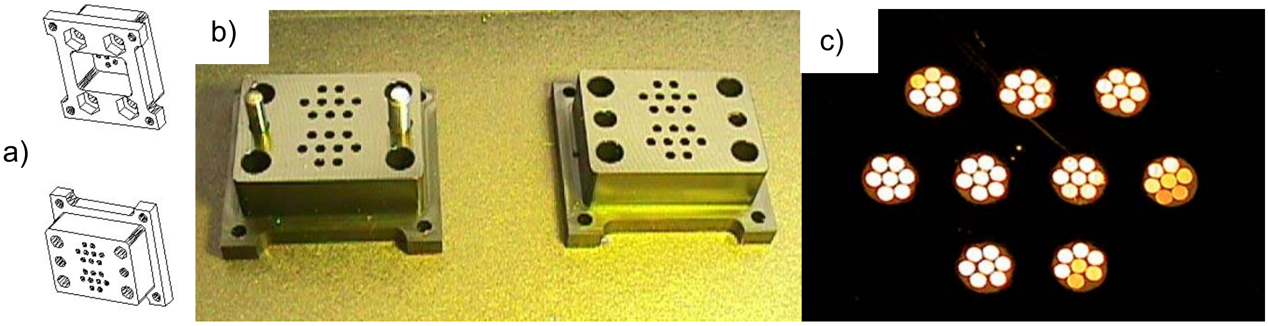

Figure 10: a) Engineering model of prototype MICE optical connector; b) Photograph of the prototype MICE optical connector; (c) Detail of sci-fi packing.

The prototype connector had the advantage that the symmetric hole-pattern allowed only one type of connector to be used for both the clear and the scintillating fibres. The disadvantage of the regular hole-pattern was that threading errors resulted from the fact that the connector had a high degree of symmetry. This issue has been addressed in the design of the optical connector for MICE.

3.5 DØ optical connectors

The optical signal from the tracker was piped to the VLPC system via clear-fibre light-guides. The light guides terminated in the DØ warm-end optical connector shown in figure 11 [8]. This is an injection-moulded part made of delrin. The typical optical throughput for this connector interface is approximately 98%. Light-guide fibre of 1.05 mm diameter was used in the prototype while the DØ cassette uses fibre of 0.965 mm diameter. This mismatch resulted in a light loss of approximately 15%.

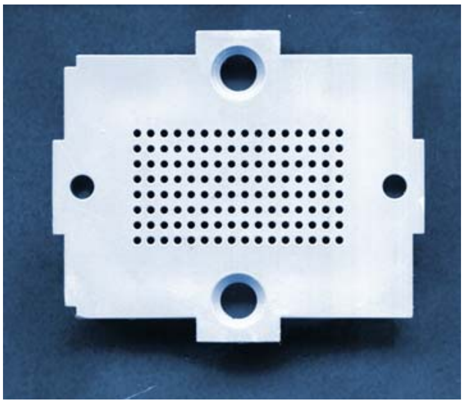

Figure 11: DØ warm-end optical connector. Shown are the 128 holes for fibres, two holes (left/right) for alignment pins and two holes (up/down) for threaded inserts.

3.6 Clear fibre light guides

The light guides were fabricated using 1.05 mm diameter clear fibre (Kuraray CLEAR-PS, round-type, multi-clad). This fibre has a tolerance of 2.5% at 3 standard deviations on the fibre diameter. The length of the light guides was 4 m. The fibre bundles were contained in an Adaplaflex PRCS28 sleeve to provide mechanical support and to exclude light. A disk was attached to the Adaplaflex sleeve to allow a light seal to be made at the end-flange of the light-box into which the stations were installed (see section 3.7).

Fibres from seven MICE connectors were routed into one 128-way DØ connector. A similar fabrication procedure to that described above was adopted for threading, potting and polishing the optical connectors of the light guides. Figure 12 shows a photograph of a completed light guide.

a) b) c)

Figure 12: Photographs of a competed clear-fibre light-guide assembly. a) The prototype MICE optical connector attached to the clear fibre. b) the fibres clad in the Adaptaflex sleeve, showing the light-excluding ring attached to the sleeve. c) The DØ optical connector. The picture shows the 'boot' that provides strain relief and mates the connector to the Adaptaflex sleeve.

3.7 Final assembly and cosmic-ray test-stand set up

A space-frame structure (shown schematically in figure 13a) was used to support the three stations. The space frame was composed of three right-angle section carbon-fibre uprights braced with twelve aluminium angle-section cross members. The whole was fixed to an aluminium base-plate. The carbon-fibre uprights were pre-moulded 1.2 mm thick carbon composites of dimension 12 mm x 12mm. The bottom end of each leg was attached to the 12 mm thick base-plate by means of a bracket and one M5 screw. The stations were attached to the uprights at the outside diameter of the station by means of small aluminium mating blocks and screws (figure 13b shows a photograph of the central station attached to the uprights in this manner). The holes through which the screws pass in the carbon-fibre uprights were elongated to allow small adjustments in their vertical orientation to be made thus allowing the stations to be positioned correctly. The three uprights were then cross-braced. The aluminium angle-section used was 12 mm x 12mm in cross section and 1 mm thick. The cross braces were held in place by means of M3 screws at their ends and attached to the uprights immediately above and below the stations (see figure 13a). Once again the holes that the screws pass through were elongated to allow angular adjustment between the stations.

a)

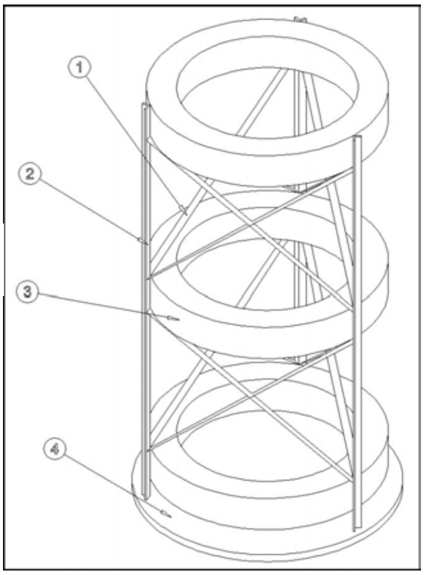

b)

Figure 13: Prototype space-frame support structure. a) Schematic diagram of the space frame. The labels indicated in the figure are: 1. cross member; 2. support leg; 3. station; 4. base plate. b) Detail of attachment of station to upright via aluminium mating blocks.

3.8 Readout electronics

3.8.1 Visible Light Photon Counter system

The MICE tracker prototype was read out using the DØ Central Fibre Tracker (CFT) optical readout and electronics system which has been operating reliably for the DØ experiment for almost 4 years [9]. The photo-detector is the Visible Light Photon Counter (VLPC) manufactured, by Boeing [10]. The VLPC is a cryogenically operated silicon-avalanche device. It is a descendant of the solid state photomultiplier, an impurity band silicon avalanche photo-detector. It has undergone six design iterations, specified as HISTE I - HISTE VI. HISTE VI, an eight element array in a two-by-four element geometry, is the version used in the DØ CFT. Each pixel in the array has a diameter of 1 mm. The HISTE VI devices used in the prototype test have the following operational parameters:

- Quantum efficiency greater that 80%;
- Gain of order 50,000;
- Operating temperature: 9K;
- Operating bias: 6-8V.

The development and operation of the VLPC has been discussed extensively in the literature [11].

The VLPC cassette contains 1024 channels of VLPC readout and is divided into 8 modules of 128 channels each of which are interchangeable and repairable. This is illustrated in figure 14. Figure 14a shows the full cassette with readout boards attached. Figure 14b shows the inner components of the cassette, with the readout boards and cassette body removed. Both figures clearly show the 8-fold modularity of the cassette design. Two analogue front-end boards (512 channel each) provide readout, temperature control and VLPC bias.

a)

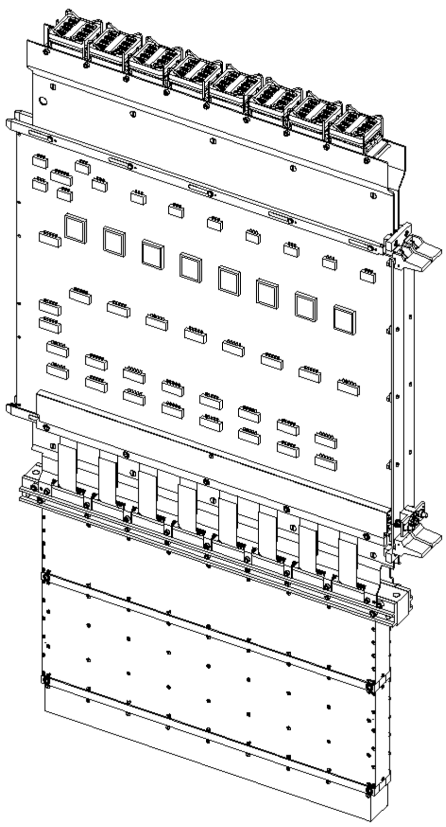

b)

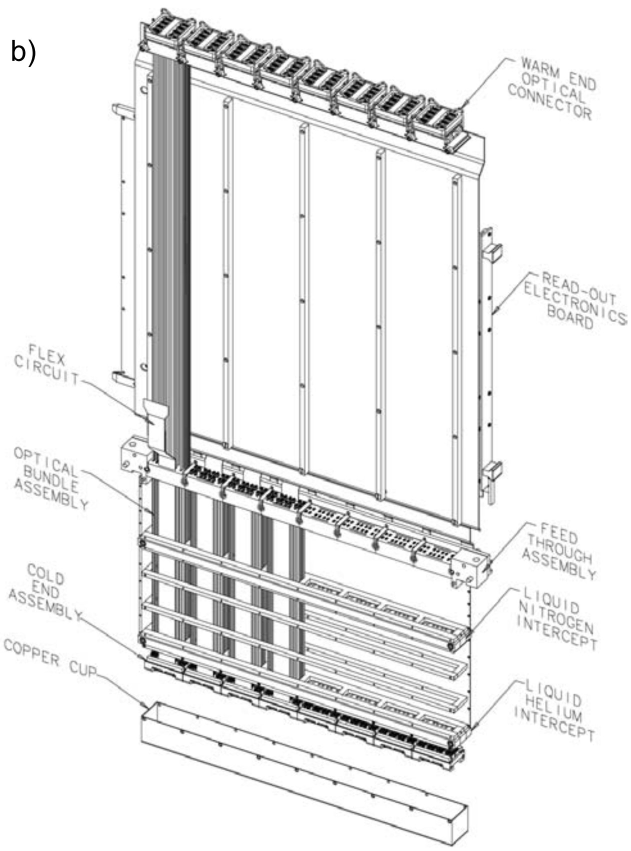

Figure 14: (a) The VLPC cassette with readout electronics board attached. (b) Inside view of the VLPC cassette with cassette body removed.

The DØ VLPC test-stand, which was used for the prototype test, consists of a four-cassette cryostat connected to the DØ central helium-liquefaction plant. Inside the cryostat, a large copper cold-sink is cooled to approximately 6 K using a flow of liquid helium. The copper cold sink sits within a stagnant volume of helium gas in which the VLPCs are immersed and cooled by conduction through the gas. The temperature stability of the cold sink is approximately ±100 mK. The 6K cold-sink temperature requires heaters in the VLPC cassette modules be used to bring the temperature of the VLPCs to the operating point of 9K. The heaters are controlled to ensure that the VLPC temperature is stable to ±25 mK.

Sitting directly over each VLPC pixel is an optical fibre which brings the light from the detector to the VLPC chip. Each cassette module is composed of an optical bundle assembly, a cold-end electronics assembly, and an assembly of mounted VLPC hybrids. The cold-end assembly is designed to be easily removable for repair without disturbing other modules due to the high cost and delicate nature of this device. Another important design requirement of this cassette regards the read-out electronics. Due to the nature of accelerator operations, the readout electronics boards and the PC boards which act as the interface to the data acquisition system must be removable and replaceable without removing a cassette from the cryostat.

The cassette is composed of several major components. The cassette is distinguished as having a "cold end", that portion of the cassette which lies within the cryostat, and a "warm end", the portion of the cassette which emerges from the cryostat and is at room temperature. At the cold end, eight cold-end assemblies each of 128 channels are hung from the feed-through by the optical bundles and are surrounded with a cold copper cup. Each cold-end assembly consists of sixteen 8 channel VLPC hybrid assemblies, the "isotherm" or base upon which they sit, the heater resistors, a temperature measurement resistor, cold-end flex circuit connectors and the required springs, fasteners and hardware. Running within the cassette body from top to bottom are eight 128 channel optical-bundle assemblies which accept light from the detector light guides connected to the warm-end optical connectors at the top of the cassette and pipe the light to the VLPCs mounted at the cold end (see figure 14b). The electronic read-out boards are located in rails which are mounted to the warm-end structure and are connected electrically with the cold-end assemblies via kapton flex circuits. In addition, the electronics boards are connected to a backplane card and backplane support structure by card-edge connectors and board-mount rails. The flex circuits and read-out boards are electrically and mechanically connected by a high density connector assembly.

The cassette body is also composed of cold-end and warm-end structures. The cold-end structure is broken down into several sub-assemblies: namely the "feed-through assembly"; the G-10 walls; the heat "intercept" assemblies and the cold-end copper cup (see figure 14a). Along the length of the cold end, two heat intercepts are integral to the cold-end cassette-structure. The first is the liquid-nitrogen (77 K) intercept which serves to cut off the flow of heat from the warm end. The second is the liquid-helium intercept which serves as a heat-radiation-suppression device and terminating structure. The warm-end structure is made of parallel aluminium plates spaced by spacer bars which form a protective box for the optical bundles.

3.8.2 Analogue Front End Board and DAQ System

The analogue front-end (AFE) board is used in DØ to read out the VLPCs [6]. Spare AFE boards were used for the MICE tracker tests. The boards mount on top of the warm end of the cassette, on either side of the optical-bundle assemblies. On each AFE, there are 8 multi-chip modules (MCMs) each serving 64 VLPC channels; so matching the construction of the cassette modules. To reduce cost and simplify the system, the front-end amplifier and digitizer used on the AFE is the same chip (the SVXIIe) that is used in the DØ silicon detector (SMT) readout. This choice allows common systems to be used further downstream in the DØ readout chain. The SVXIIe and its readout are described elsewhere [12]. On the AFE, the SVX chip integrates the charge signals from the VLPCs; provides pipelined storage of the signals while a trigger is formed; digitises the signals; and reduces the volume of data to be recorded through a zero-suppression algorithm (sparsification). There are 8 SVX chips on each AFE board; one on each MCM. The AFE also provides the bias for, and the temperature control of, the VLPCs. For the prototype test, the AFE was operated through a stand alone sequencer (SASEQ). These modules are used by DØ to test and commission SVX-based electronics. This choice allowed a small stand-alone system to be assembled from existing components. The DAQ system consisted of one VME crate with a SASEQ and a MIL1553 module [13] to interface the system to a PC. The control of the VLPC bias and temperature was accomplished through the MIL1553 interface via the AFE board. The readout of the VLPC data was performed by triggering the SASEQ with a cosmic ray scintillation-counter telescope and reading out the data from the SASEQ via VME to the PC and recording it to disk for later analysis. The AFEs digitise analogue signals with a noise equivalent to a signal of ~0.6 photo-electrons. Calibration of the system is performed using an LED. Figure 15 shows a typical calibration spectrum in which the pedestal and 1, 2, and 3 photo-electron peaks can clearly be seen. The clear separation of the photo-electron peaks allows individual channel thresholds to be reliably set.

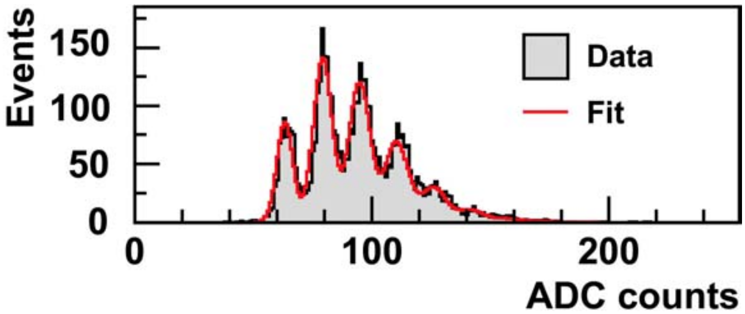

Figure 15: Typical LED-calibration spectrum for one VLPC taken during the MICE prototype tracker data taking period in the DØ cosmic ray test stand. The shaded histogram is the measured pulse height spectrum. The solid red line shows the fit to the data. The pedestal, one-, two- and three-photoelectron peaks are clearly visible.

The trigger for prototype test was formed from two pairs of scintillator paddles placed directly above and below the tracker cylinder. A layer of lead bricks approximately 10cm thick was placed between the tracker and the lower paddles to ensure that the trigger only fired for muons with energies above ~2 MeV in the tracker volume. Since the DØ electronics are designed to be used in a collider environment, the cosmic-ray trigger for the prototype test was gated to match the pattern of activity generated in the AFE boards by the Tevatron colliding-bunch structure [14]. A trigger was accepted only if the AFE boards were able to integrate completely any VLPC signals corresponding to the transit of a muon through the tracker volume. This reduced the efficiency of the cosmic trigger, but greatly simplified the analysis of the data.

4. Measurement of the intrinsic properties of the fibre

A programme to measure the intrinsic properties of both the clear and the scintillating fibre to be used in the MICE scintillating-fibre tracker is underway. The first in a series of light-yield and cross-talk measurements has been performed in test beams at KEK. These data are presently being analysed and a second data-taking period is being planned. The attenuation in the clear-fibre light-guides was measured; these measurements are described below and used in section 6 to evaluate the light yield to be expected from the prototype tracker in the cosmic-ray test stand at DØ.

4.1 Measurement of attenuation length of clear fibre

The attenuation in the clear-fibre light guides was measured using a light-emitting diode and optical sphere (diffuser) at Fermilab. The measurement system, which consisted of an optical sphere instrumented with a silicon photo-detector, was provided by Oriel [15]. Figure 16 shows a schematic view of the setup. A length of scintillating fibre of the type to be used in the MICE tracker was excited using a blue light emitting diode (LED). The wavelength of the injected light was shifted by the secondary fluor, 3HF, so that green light was injected into a length of clear fibre that was attached to the scintillating fibre. The LED was driven at 100 Hz by a pulse generator with a 5.5 V pulse-height. The light emitted by the LED was monitored by the reference photo-detector of the system. The light emerging from the scintillating fibre was led via a length of clear fibre to the optical sphere. Random reflections inside the sphere serve to ensure that light leaving the clear fibre in any direction is sampled by the photo-detector. The luminosity of the diffused light was measured using the 'signal' silicon photo-detector attached to the sphere. Comparison of the response of the signal photo-detector with that of the reference photo-detector allowed the stability of the LED to be determined pulse-by-pulse. To avoid uncertainties arising at the optical interfaces (LED-scintillating fibre and scintillating-clear fibre) a series of measurements was made using ever shorter lengths of clear fibre. Initially, an 8 m length of clear fibre was prepared and a light-transmission measurement made. A series of light-transmission measurements was then made with the clear-fibre light guide shortened by 0.5 m between subsequent measurements. Care was taken not to disturb the scintillating/clear-fibre junction when the fibre was cut. The end of the fibre was carefully polished using a diamond cutter before being re-attached to the optical sphere.

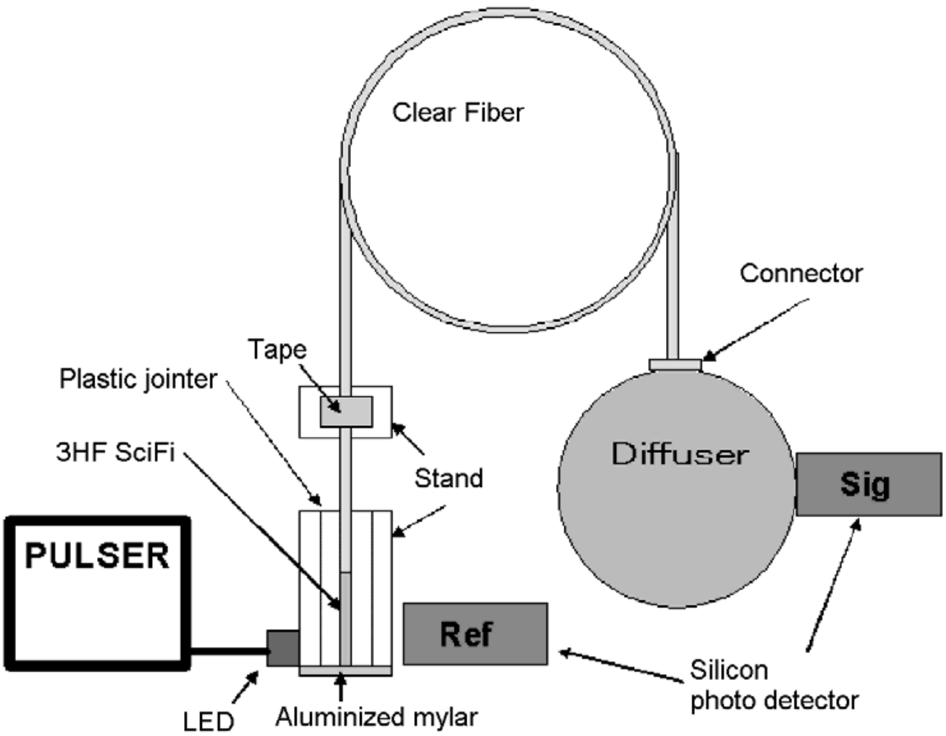

Figure 16: Schematic diagram of set up used to measure attenuation of clear fibre.

For each length of clear-fibre, a measurement of the pulse height in the signal photo-detector (s) and the reference photo-detector (r) was made. Figure 17 shows a plot of the ratio s/r as a function of the clear-fibre length. The transmitted luminosity appears to fall exponentially. The attenuation length of the fibre was determined by fitting the function

$$\frac{s}{r} = \exp(\alpha_1 - \lambda_1 l) + \exp(\alpha_2 - \lambda_2 l)$$

where l is the length of clear fibre, α_1 and α_2 are amplitude coefficients and λ_1 and λ_2 are the attenuation lengths. The result of the fit is shown in figure 17. The values of the short and long attenuation lengths determined are: $\lambda_1 = 0.69\,\mathrm{m}$; and $\lambda_2 = 7.6\,\mathrm{m}$. In the case of the 4 m light guides used in the prototype test, half of the injected light will reach the VLPC.

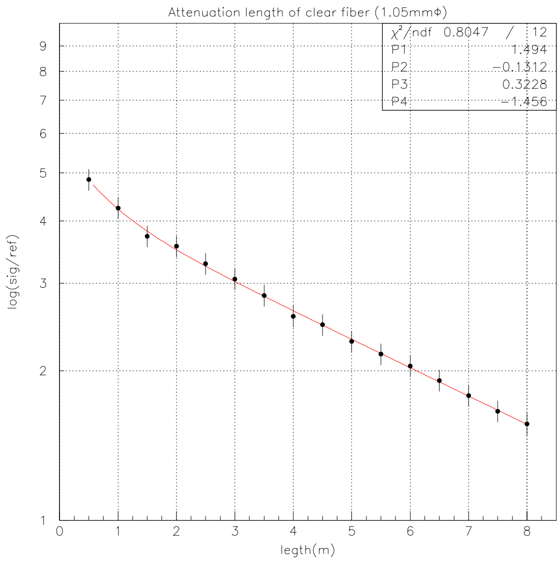

Figure 17: The result of attenuation measurement in clear fibre. The horizontal axis shows the length of clear fibre; the measured luminosity after transmission through the clear fibre with respect to the light yield of the LED source is shown on the vertical scale.

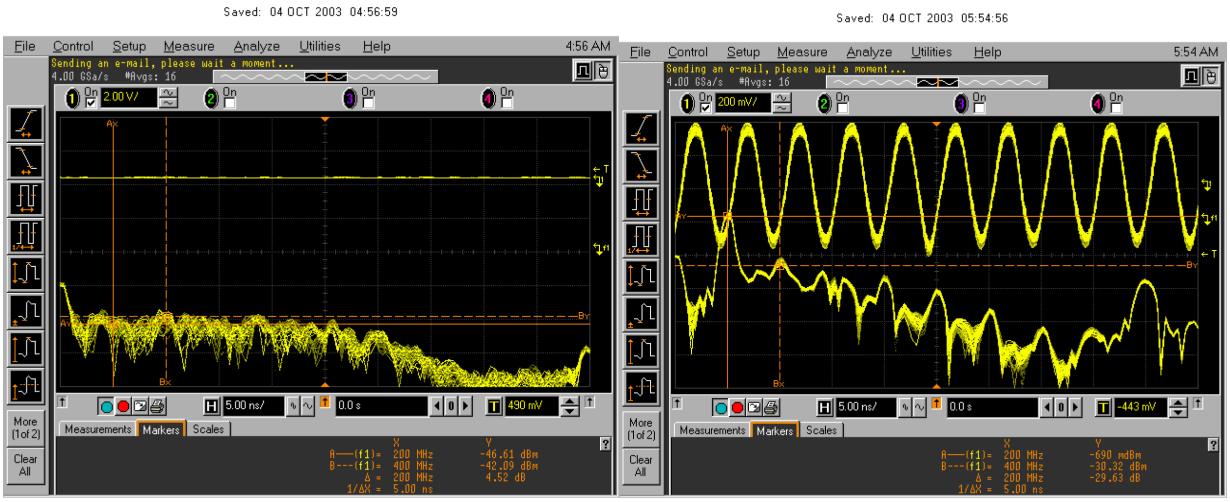

Figure 18: Oscilloscope traces showing the radiated RF power observed at the location of the DØ VLPC test stand. The screen capture on the left-hand side was recorded with the RF source turned off. The top trace shows the RF signal recorded by the receiving antenna. The bottom trace shows the Fourier transform of the signal received. The screen capture on the right-hand side shows the 201 MHz signal received by the antenna (top trace) when the transmitter was set to maximum power (+10 dB). The bottom trace is the Fourier transform of the top trace and shows a strong peak at 201 MHz.

5. Effect of radio-frequency noise on the electronics

The MICE tracker and the associated readout electronics are required to operate in the vicinity of high-gradient accelerating cavities and a high-power-RF supply and distribution system. It is therefore important to determine the response of the readout electronics to RF power leaking from the cavities, the power supplies and the power-distribution system.

To estimate the effect that radiated RF power will have on the VLPC readout electronics, an RF generator was used to irradiate the DØ test stand. The test stand was subjected to 201 MHz radiation at various power levels. An antenna was placed next to the cryostat and the received power was recorded on a digital oscilloscope (see figure 18).

The VLPC system was set up with a random trigger and with all optical inputs covered to ensure that no light reached the VLPCs. Pedestal data was recorded for a variety of radiated power settings and antenna orientations. Data were taken with the transmitting antenna placed vertically and horizontally, to ensure that any polarisation dependant reception in the electronics would be detected. The radiated RF power was varied between -7 dB and +10 dB. For each power setting and transmitting-antenna position, the pedestal position and width were measured for each of the 1024 channels. In the worst case, the pedestal width increased by 0.5 ADC counts or approximately 0.033 photo-electrons.

6 Reconstruction and analysis of cosmic ray tracks

6.1 Reconstruction

The stages in the track reconstruction were:

- Identification of hits on individual VLPC channels and the association of these hits with the appropriate group of seven scintillating fibres (hit finding);
- Association of hits on neighbouring groups of seven fibres (clustering);
- Reconstruction of space points in the planes of one station (space-point reconstruction);
- Pattern recognition among the space points reconstructed in the three stations of the prototype to give track candidates. The space points associated to a track were fitted to a straight line to determine the track parameters.

The reconstructed objects listed above were used to determine the point resolution, the light yield, the single-plane efficiency and the dead-channel rate.

6.1.1 Hit finding

In the DØ test stand, only one VLPC cassette (1024 channels) was available to read out the prototype tracker. As a result, only a subset of the 1512 groups of 7 fibres that comprise the 7 tracking planes could be instrumented. The central region of each plane was read out as shown in figure 19. Each channel was calibrated by determining the pedestal position and width using data taken with the cosmic ray trigger. The channel-by-channel gain was determined in dedicated runs in which the VLPCs were excited using an LED pulser (see section 3.8.2). Common mode noise was determined (at the MCM) and subtracted. A hit was defined to be a signal corresponding to at least one photo-electron (PE).

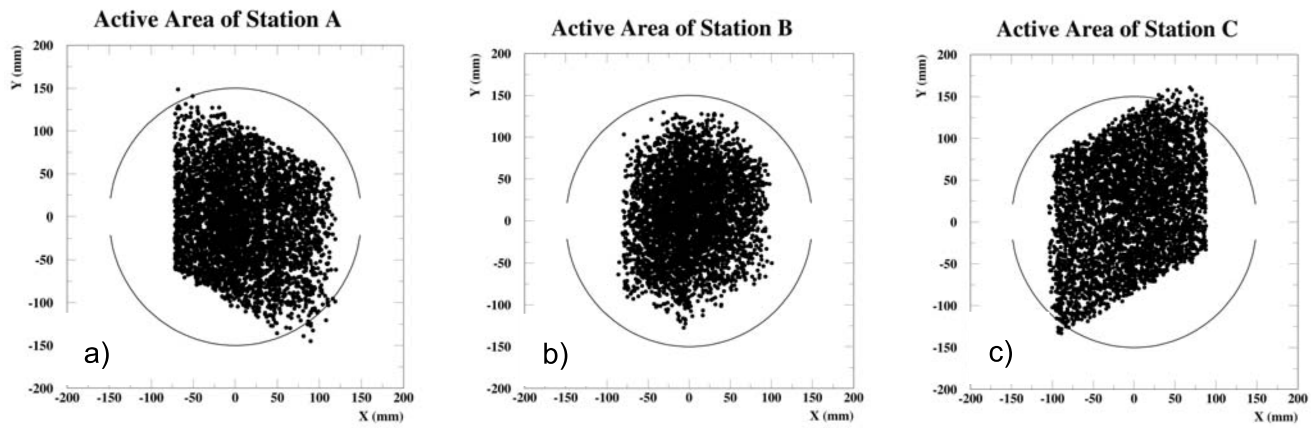

Figure 19: Regions of prototype read out in prototype test.

6.1.2 Cluster finding

A particle passing through the boundary between one group of seven fibres and the next may generate light in both groups. In such a case, two neighbouring hits will be reconstructed in the hit-finding phase. A search for clusters of hit fibres was performed to group neighbouring hits into clusters. All hits found as described in section 6.1 are considered in the cluster search.

The cluster search proceeds as follows. Isolated hits with a pulse height of at least 2 PE were considered to be a cluster. Two neighbouring hits for which the sum of the individual pulse height was greater than 2 PE were grouped to form a cluster. The cluster centre was taken to be the pulse-height weighted mean of the two hit positions. As a result of this procedure, all clusters have a combined signal of at least 2 PE, a signal that corresponds to ~3 times the typical width of the pedestal.

6.1.3 Space-point reconstruction

Stations A and C each measure only two projections while station B, with three doublet layers, measures all three projections. Hence, only a two-fold coincidence (a duplet) can be found in stations A and C while a three-fold coincidence (a triplet) or a duplet can be found in station B. All combinations of clusters in the three projections of Station B were first considered. An internal residual, which measures the difference between the X position determined by the intersection of the V and W planes with that defined by the X plane was computed. The combination of clusters with the smallest internal residual was kept so long as that residual is less than 2 mm. The coordinates of the space point were calculated and the clusters used were 'locked off', i.e. removed from the list of clusters to be searched. Once all triplet space points had been found, all combinations of pairs of clusters in different projections of the same station were used to make a space point. All space points that lay within the active region of the scintillating fibre were retained.

6.1.4 Track reconstruction

A search is made over all combinations of three space points (one in each of the three stations) to find the combination that gives the smallest χ^2 when fitted to a straight line. Figure 20 shows a typical event in which a track is reconstructed.

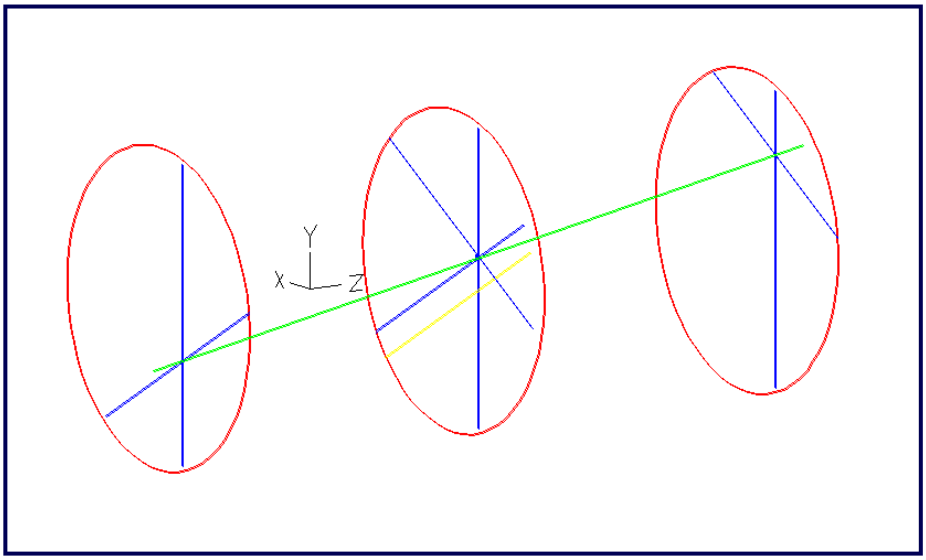

Figure 20: Event display showing a typical cosmic ray track reconstructed in the MICE fibre-tracker prototype. The clusters that 'belong' to the reconstructed track are shown by the blue lines while the active areas of the stations themselves are indicated by the red circles. The track is indicated by the green line. The yellow line in station B indicates an additional cluster with a signal above 2 PE that was not associated with a track.

6.2 Analysis of cosmic-ray data

The cosmic-ray data were analysed to extract the point resolution, the light yield, the single-plane efficiency, and the dead-channel rate.

6.2.1 Resolution

The resolution was determined using events in which a track had been reconstructed. Information from the X projections in each of the 3 stations was used. The position at which a cluster in a given station was expected was determined using the other two stations. The predicted position in stations A or C was determined by extrapolation while the predicted position in station B was determined by interpolation. The width of the distribution of residuals (predicted cluster position minus observed cluster position) was determined. The resolution to be attributed to the fibre doublet is determined by subtracting (in quadrature) the uncertainty introduced by the extrapolation or interpolation described above. The doublet-layer resolution determined in this way is 442 ± 4 (stat) ± 27 (syst) μm. The systematic error was determined from the difference between the estimation of the resolution determined in station A, B and C.

The expected resolution can be determined from the known fibre pitch and the fibre-ganging scheme. Neglecting the effects of multiple scattering (which should be small due to the momentum filter in the cosmic ray trigger) and taking into account variations in the geometry of tracks passing through the tracker, the resolution would be expected to lie between 424 μm and 465 μm, in agreement with the measurement.

6.2.2 Light yield

Using only events that contained a reconstructed cosmic-ray track, the light yield was determined as a function of the 3HF concentration by plotting the pulse height for each of the doublet layers that contained fibres with the same concentration. Data from the doublet layer which contained a variety of 3HF dopings were not used. A Gaussian fit was made to the peak of the distribution to determine the most probable yield. The light yield was taken to be the most probable value determined in this way.

Figure 21 shows the pulse-height distribution obtained for each of the three 3HF concentrations used. The data are compared to a Monte Carlo simulation of the prototype tracker. The simulated pulse-height distributions were obtained using G4MICE [18] as follows:

i. G4MICE was used to calculate the distribution of energy lost in a doublet layer;

ii. A multiplicative factor to convert the energy deposited in the fibre into an expected number of photo-electrons was determined by comparing the mean of the generated energy-loss distribution to the mean of the measured pulse-height distribution;

iii. G4MICE was then used to convolute the energy loss distribution with the Poisson photo-statistics distribution. Event-by-event the energy deposited in a doublet layer was converted to an expected mean number of photo electrons ($\langle n_{\mathrm{exp}} \rangle$) using the multiplicative factor determined in ii. The simulated number of photo electrons was then obtained by sampling the Poisson distribution with a mean of $\langle n_{\mathrm{exp}} \rangle$;

The simulation gives a reasonable description of the data. The light-yield results are summarized in table 2.

6.2.3 Double-layer efficiency

The doublet-layer efficiency was determined using station B. A search for tracks was made using stations A and C as well as two of the three projections of station B; the third plane in station B being the plane for which the efficiency was to be determined. The track with the lowest χ^2 was used. The track was then extrapolated to the plane under investigation and the perpendicular distance from the extrapolation to the nearest cluster is determined. If this distance was less than a given road-width, a 'success' was recorded. In all cases when an extrapolation was performed, an 'attempt' was recorded. The efficiency of a plane was determined as the ratio of successes to attempts. The efficiency as a function of 3HF concentration is shown in table 3. Table 3 also shows the efficiency that would be expected based on the Poisson distribution with the most probable light yields presented in table 2. The results show good agreement between the efficiency determined from tracks and that expected on the basis of light yield.

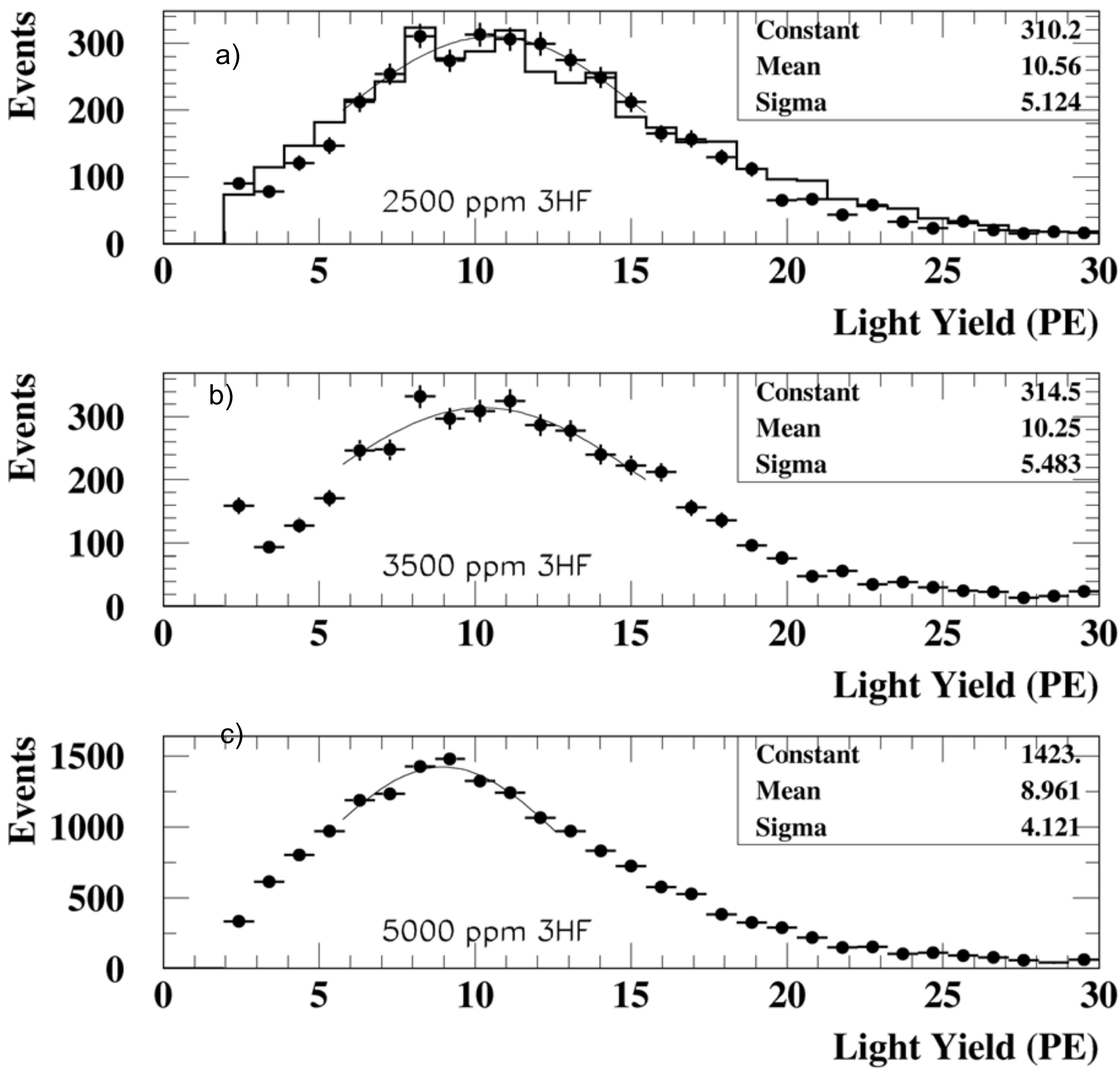

Figure 21: Pulse height distributions: (a) 2500 ppm 3HF; (b) 3500 ppm 3HF; (c) 5000 ppm 3HF. The data are shown as the points. The result of a Gaussian fit to the peak is shown as the solid line. The mean of the Gaussian distribution is noted. In (a), the histogram is the result of the simulation described in the text.

3HF Concentration (ppm)	Most Probable Light Yield (PE)
2500	10.6 ± 0.2
3500	10.3 ± 0.1
5000	8.96 ± 0.06

Table 2: Summary of measurements of light yield as a function of 3HF concentration.

3HF Concentration (ppm)	Measured Efficiency (%)	Expected Efficiency (%)
2500	99.7 ± 0.2 (stat.)	99.7 (10PE)
3500	99.3 ± 0.3 (stat.)	99.7 (10PE)
5000	98.1 ± 0.4 (stat.)	98.6 - 99.4 (8-9PE)

Table 3: Efficiency measured using tracks compared to the efficiency expected on the basis of Poisson distributions with the most probable photo electron yields reported in table 2.

6.2.4 Dead channel rate

A dead channel is taken to be a channel for which the number of hits with pulse height above 4 PE is very low compared to neighbouring channels. One channel was found with a very low rate, a second was found with a lower rate than its neighbours. The worst case, is therefore 2 bad channels out of 1008 read out which is 0.2%. This is to be compared with the dead-channel rate in the DØ fibre tracker which is 0.25% [7]. Once the test-run was complete, the tracker was disassembled. The optical connector on the station that corresponded to the one completely dead channel was observed to be plugged with Araldite. The second dead channel, with the significantly reduced light yield, was also observed to have an Araldite plug at the station connector that obscured three of the seven fibres that should have delivered light to this channel. The quality-assurance procedures being developed for the final manufacturing process will be capable of revealing such errors.

7. Simulation of full tracker in G4MICE

In this section, the simulation, digitisation and reconstruction of the full scintillating-fibre tracking system for MICE using the G4MICE software package is presented. A discussion of the results relevant to the performance of the device is given in section 7.4.

7.1 Simulation

The material description in G4MICE includes the scintillating fibre doublet layers, the glue that holds the layers together, the mylar film and a simplified model of the carbon fibre support. The scintillating fibres are modelled in GEANT4 as a series of individual fibres, each of which is described by a number of cylinders, one inside the other, representing the core and the cladding of the fibre. The passage of a particle through any of the fibres results in a “hit” being recorded. Each hit includes such information as the position, momentum, energy deposited and time of passage, as well as the type of particle.

7.2 Digitisation

The digitisation executable reads in the simulated hit information, described in Section 7.1, and produces a set of digitised responses from the VLPC system. The digitisation uses parameterisations to simulate the light production, conversion, trapping efficiency, propagation along the fibre, transport to the VLPC, response of the VLPC and that of the read-out electronics. The parameters used to describe each of these processes has been chosen based on the experience of the DØ experiment, and subsequently tuned to match the results obtained from the tracker prototype. Figure 21a shows the agreement between the simulated response of the fibre tracker and the light yield obtained from the prototype.

7.3 Reconstruction

The reconstruction has 4 main stages: cluster building; space-point reconstruction; track finding; and Kalman fitting; each will be described in turn.

7.3.1 Cluster building

A particle passing through the boundary between one group of seven fibres and the next may generate light in both groups. In such a case, two neighbouring hits will be reconstructed in the hit-finding phase. A search for clusters of hit fibres was performed to group neighbouring hits into clusters. All hits found as described in section 6.1 are considered in the cluster search.

The first stage of reconstruction builds clusters from the digitised hits. In some events, a track will pass through the boundary between one group of seven fibres and the next, so generating light in two neighbouring VLPC channels. A limitation in the software design results in each of the seven fibres within a bundle of seven generating a hit. As a result, the cluster building software starts by calculating the signal on each VLPC channel by summing the signals generated by each of the seven scintillating fibres associated with the channel. The same process is then repeated for the VLPC channel corresponding to the neighbouring cluster of 7 fibres, in case the track passed through this overlap region. If a single VLPC channel has a signal of more than 2 PE, or two neighbouring channels each have a signal of at least 1 PE (the same criteria as were used in the analysis of the data from the prototype) a cluster is made from the sum of all the digitisations.

7.3.2 Space point reconstruction

The space point reconstruction currently builds "triplets" which consist of a cluster in each of the three views of a given station. A χ^2 is formed from the internal residual of the reconstructed position from two clusters and that of the third and the difference in the time measured from each of the three clusters. In the future, space points consisting of two clusters will also be provided in order to increase the space-point efficiency.

7.3.4 Track finding

The pattern recognition stars by searching for collections of 3 points for which the helix parameters can be determined analytically. If the total momentum is within a plausible range, and the reconstructed times of each of the 3 points are consistent with a particle travelling downstream, the combination is kept for consideration. The track parameters derived from each of these sets is used to search for matching space points in the remaining two stations. In each case, the residual in position and time is used to select the best candidate. For each set of 4 or 5 space points that have been selected, a track fit is made using the Kalman filter (see section 7.3.5) and the candidate with the lowest χ^2 is kept.

7.3.5 Kalman fitting

The Kalman filter used is that provided by the "RecPack" package [16]. The filter allows a magnetic field map to be provided for the propagation of states through the experiment, as well as a user-definable model for dE/dx which has a significant effect on 200 MeV/c muons as they pass through the detector.

7.4 Performance

The performance of the tracker has been studied using the G4MICE package under the following conditions:

- Input beam description: the "June04" description of the MICE Muon Beam [17], simulated using the G4BeamLine [18] and TURTLE [19] packages;
- RF background description: the version of the code presented at the 22nd September 2004 MICE video meeting [20];
- The nominal station spacing, ganging [3], and digitisation based on the results of the tracker prototype.

7.4.1 Emittance reconstruction

7.4.1.1 Specification

The specification for the tracking device, presented in the MICE proposal [2] and in the tracker technology-choice document [4] is that the resolution in the variables from which the six-dimensional emittance is calculated must be less than 10% of the RMS width of the distribution of the same variable at equilibrium emittance. The argument by which this specification was arrived at was presented in [21] and is briefly recalled here.

Assume that, in the i^{th} variable, the true RMS spread of the beam is σ_i^{true} and that the RMS resolution of the tracker in the i^{th} variable is σ_i^{res}. The RMS spread of the measured distribution of i (σ_i^{meas}) is given by:

$$\left(\sigma_i^{\mathrm{true}}\right)^2 = \left(\sigma_i^{\mathrm{meas}}\right)^2 - \left(\sigma_i^{\mathrm{res}}\right)^2 . \tag{1}$$

The uncertainty in the measurement causes a bias in the measured width of the beam, σ_i^{meas}. To estimate the bias, equation 1 can be rearranged as follows:

$$\sigma_i^{\mathrm{meas}} = \sigma_i^{\mathrm{true}} \sqrt{1 + \left(\frac{\sigma_i^{\mathrm{res}}}{\sigma_i^{\mathrm{true}}}\right)^2} \approx \sigma_i^{\mathrm{true}} \left(1 + \frac{1}{2}\left(\frac{\sigma_i^{\mathrm{res}}}{\sigma_i^{\mathrm{true}}}\right)^2\right), \tag{2}$$

where the binomial expansion has been used to obtain the approximate expression. In order for the bias in σ_i^{meas} to be less than 1%

$$\frac{\sigma_i^{\mathrm{res}}}{\sigma_i^{\mathrm{true}}} \leq \frac{1}{7} \approx 14\% . \tag{3}$$

The figure of merit chosen, $\sigma_i^{\mathrm{res}} / \sigma_i^{\mathrm{true}} \leq 10\%$ satisfies 3. Note that in this analysis, correlations between the measurement uncertainties and the particle coordinates have been ignored as have correlations between the measured parameters themselves. A more detailed discussion of the emittance-correction procedure follows [22].

7.4.1.2 Correcting the measured emittance

In $2 \times n$ dimensions, the true normalised emittance is given by:

$$\varepsilon_{2nN} = \frac{1}{m_\mu} \sqrt[2n]{\left|V_{2n}^{\mathrm{true}}\right|} \tag{4}$$

where V_{2n}^{true} is the true covariance matrix of the $2n$ muon-beam phase-space parameters and m_μ is the muon mass. The elements of V_{2n}^{true} are given by:

$$\left(V_{2n}^{\mathrm{true}}\right)_{ij} = \left\langle \left(w_i - \overline{w}_i\right)\left(w_j - \overline{w}_j\right) \right\rangle \tag{5}$$

where w_i is the true value of the i^{th} phase-space variable and $\overline{w_i}$ is the mean of w_i over the particles in the beam. The measured value of the same variable m_i is related to w_i by:

$$w_i = m_i + \delta_i , \tag{6}$$

where δ_i is a small increment. Substituting in equation 5, the expression for V_{2n}^{true} becomes:

$$\left(V_{2n}^{\mathrm{true}}\right)_{ij} = \left\langle \left(m_i - \overline{m}_i\right)\left(m_j - \overline{m}_j\right) \right\rangle - \left\langle \left(m_i - \overline{m}_i\right)\left(\delta_j - \overline{\delta}_j\right) \right\rangle - \left\langle \left(\delta_i - \overline{\delta}_i\right)\left(m_j - \overline{m}_j\right) \right\rangle - \left\langle \left(\delta_i - \overline{\delta}_i\right)\left(\delta_j - \overline{\delta}_j\right) \right\rangle \quad (7).$$

Defining the covariance matrix of the measured track parameters by:

$$C_{ij} = \left\langle \left(\delta_i - \overline{\delta}_i\right)\left(\delta_j - \overline{\delta}_j\right) \right\rangle \tag{8}$$

and the correlation matrix between the measured phase-space coordinates and the fluctuations in the measurements by:

$$R_{ij} = \left\langle (m_i - \overline{m}_i)(\delta_j - \overline{\delta}_j) \right\rangle \tag{9}$$

the expression for V_{2n}^{true} (equation 7) becomes:

$$V_{2n}^{\text{true}} = V_{2n}^{\text{meas}} - R - R^T - C \,. \tag{10}$$

Note that *R* is not a symmetric matrix but $R + R^T$ is. G4MICE was used to calculate *R* and *C* so that the correction could be applied to the simulated data.

7.4.2 Tracker performance

The spatial resolution of the fitted tracks is illustrated in figure 25. Figures 25a and b show the distribution of the difference between the fitted position of the reconstructed track and the true position at the reference surface (specified to be in the centre of the singlet layer closest to the liquid-hydrogen absorber [3]) in the two special coordinates transverse to the spectrometer axis. The RMS width of the *x*-difference distribution is 347 μm. The *y* position is reconstructed from the single doublet-layer the fibres of which run parallel to the *x* axis. The flat distribution reflects the flat seven-fold ganging of the scintillating fibres. The RMS spread of this distribution is 370 μm. The resolution in the momentum components transverse to the beam axis is shown in figures 25c and d. Figure 22 shows the resolution in p_T as a function of p_T and p_z and the resolution in p_z as a function of p_T and p_z.

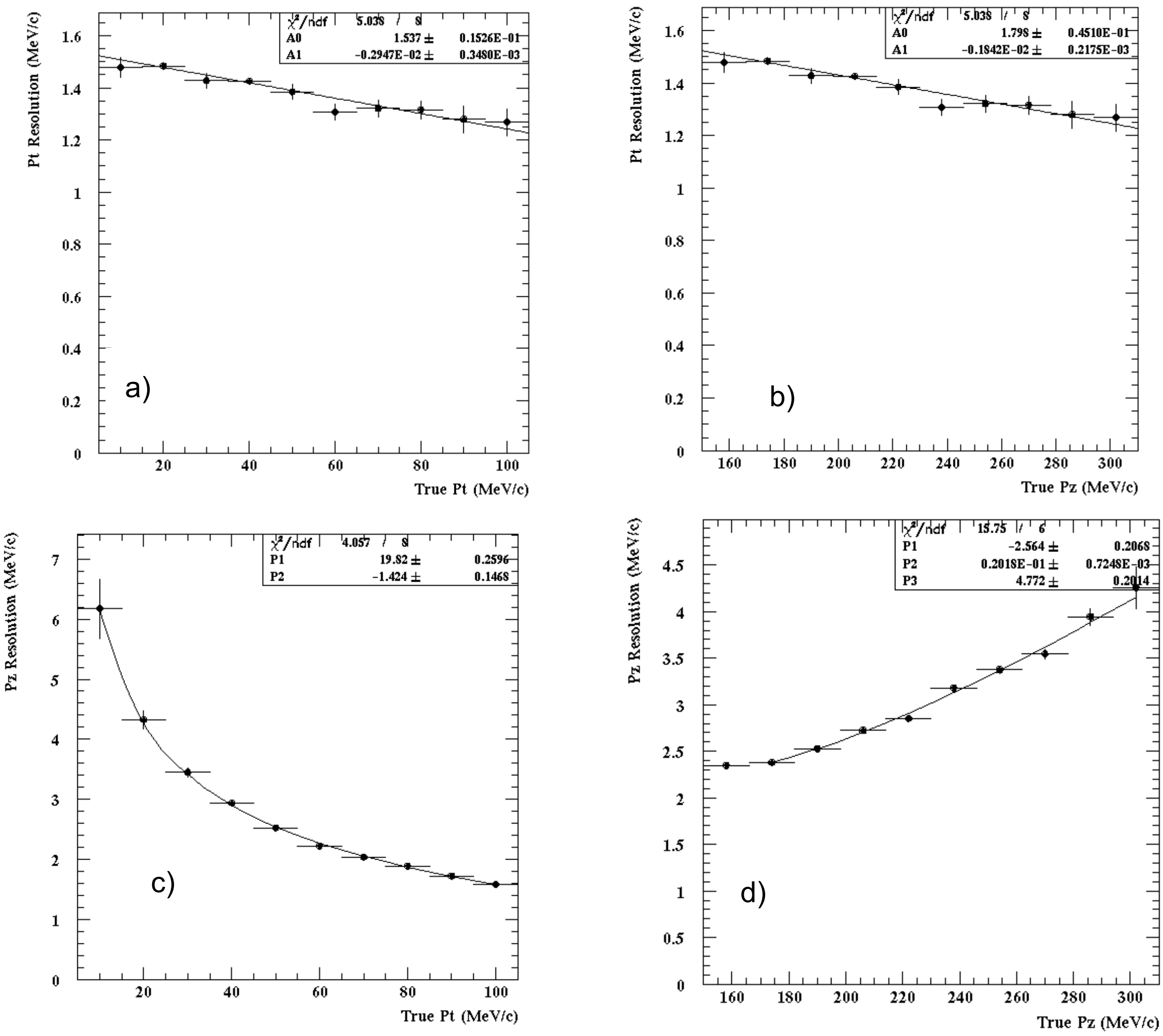

Figure 22: The resolution in p_T is shown *as a function of* p_T in (a) *and as a function of* p_z in (b). *The resolution in* p_z *is shown as a function of* p_T *in (c) and as a function of* p_z *in (d).*

Figure 23 shows the track finding efficiency as a function of p_T, p_T/p_z and p_z for the upstream (input) and downstream (output) tracker.

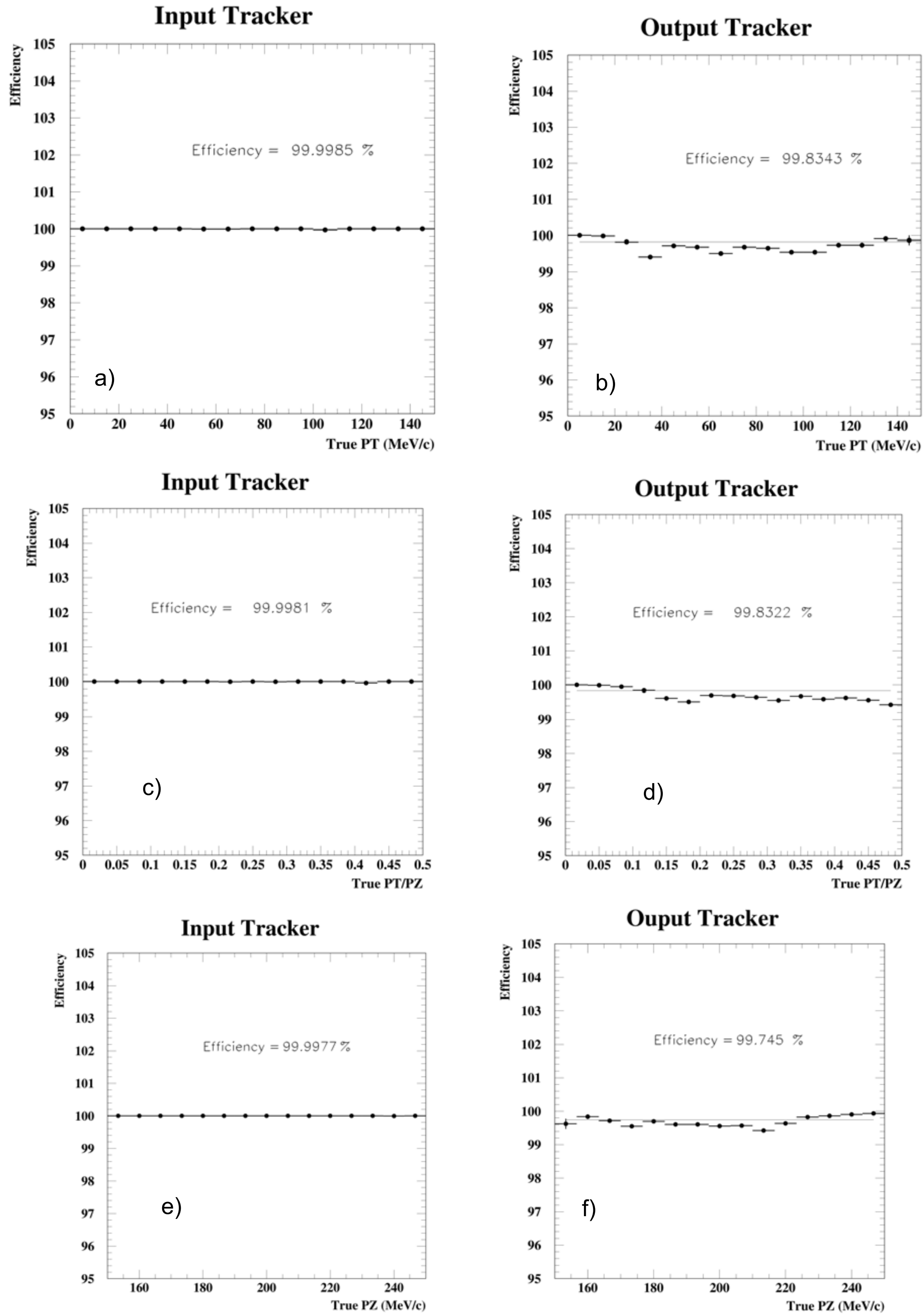

Figure 23: Track finding efficiency for the upstream (input) and downstream (output) tracker as a function of p_T *(a and b);* p_T/p_z *(c and d); and* p_z (e and f).

Figure 24 shows the track purity (defined as the fraction of hits in the track that were produced by a muon) as a function of p_T, p_T/p_z and p_z for the upstream (input) and downstream (output) tracker.

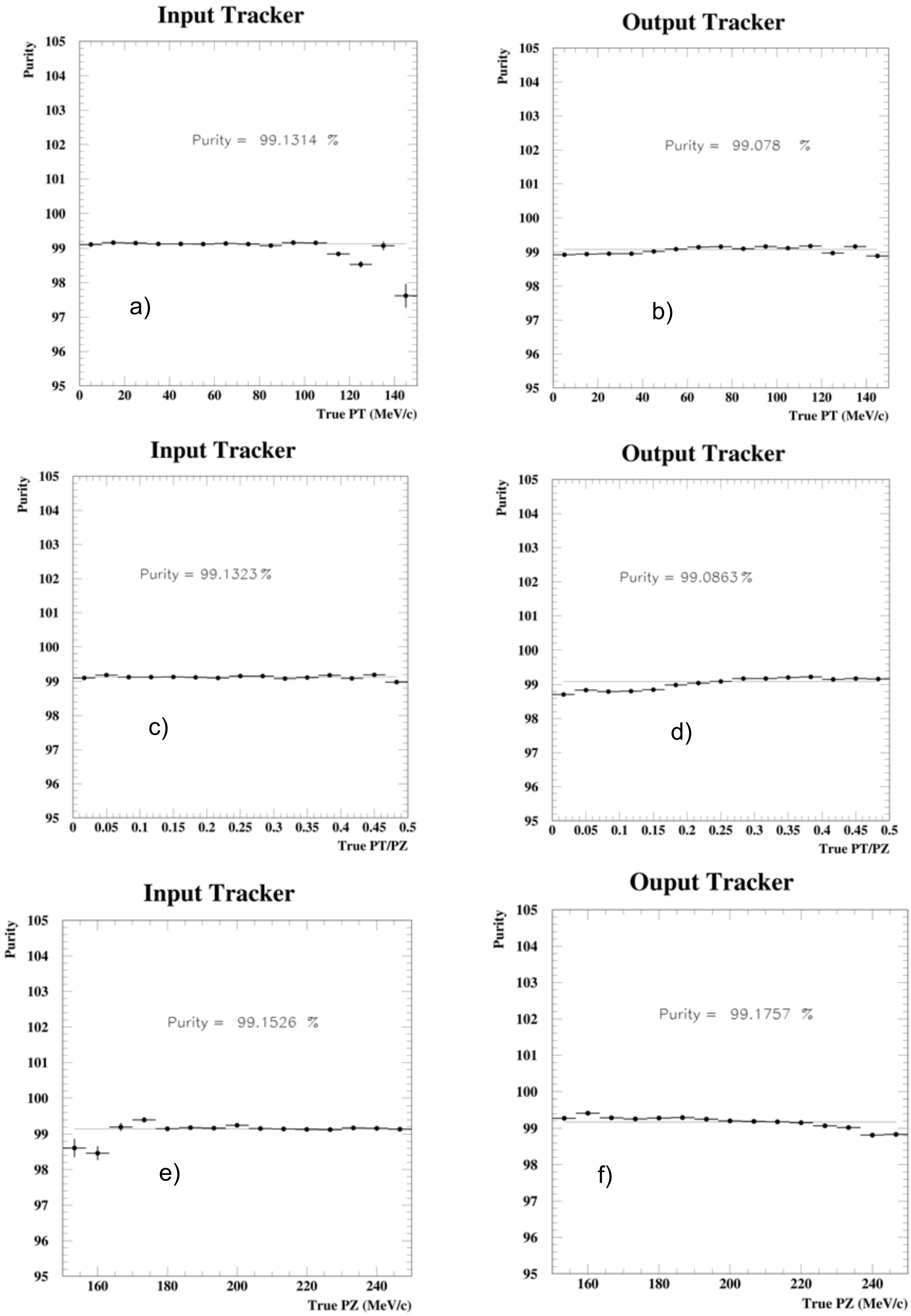

Figure 24: Hit purity (defined as the fraction of hits in the track that were produced by a muon) for the tracks found in the upstream (input) and downstream (output) tracker as a function of p_T *(a and b);* p_T/p_z *(c and d); and* p_z (e and f).

7.4.2.1 Four-dimensional, transverse, emittance

The normalised four-dimensional emittance, ε_{4N}, is defined by [3]

$$\varepsilon_{4N} = \frac{1}{m_\mu}\sqrt[4]{|V_4|}$$

where V_4 is the covariance matrix of the x, p_x, y, p_y distributions of the muon beam. To assess the degree to which the tracker meets the specification, the measured RMS resolution values of each of the phase-space coordinates x, p_x, y, p_y must be compared to the RMS spread of the same variable using an equilibrium emittance (2.5 π mm rad) beam.

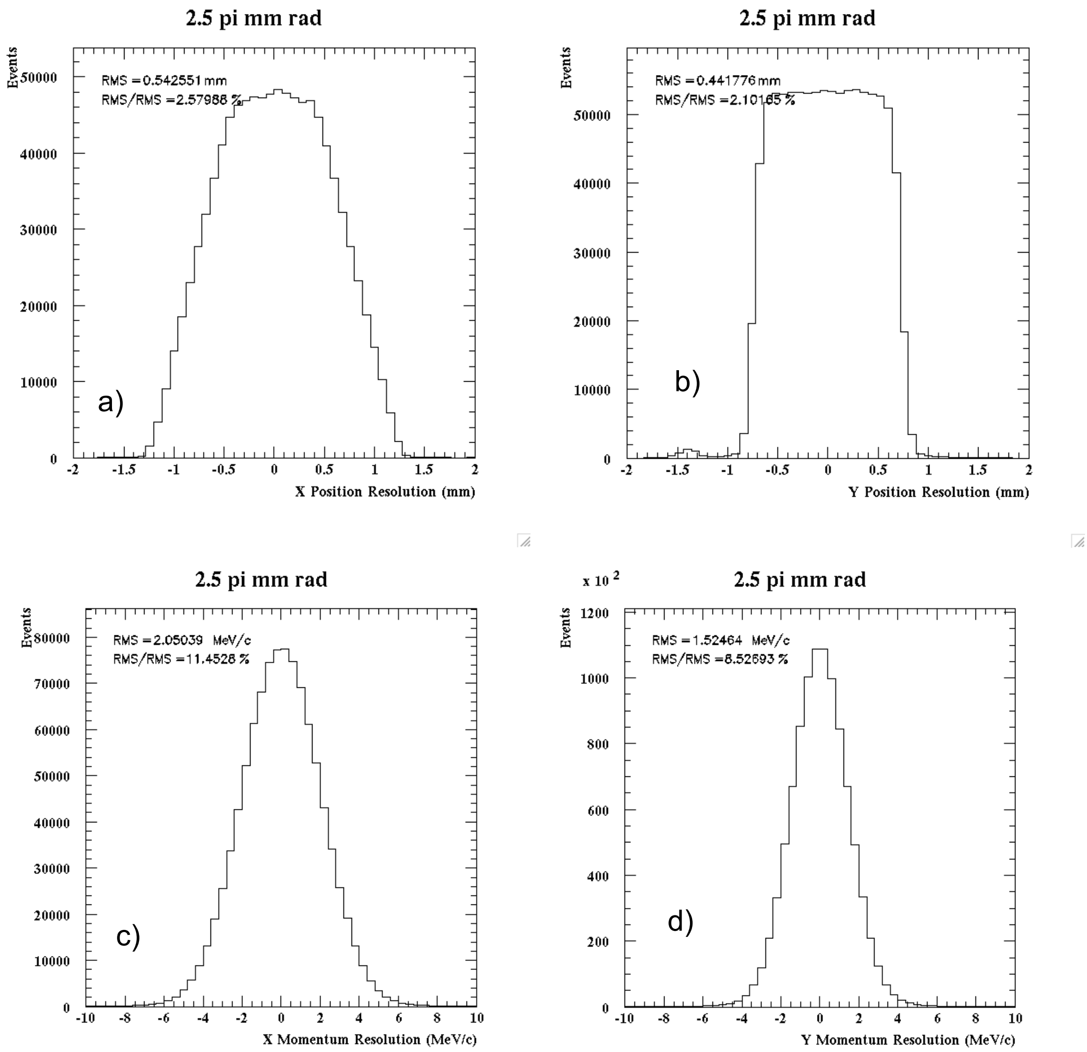

Figure 25: Resolution in transverse phase-space coordinates reconstructed using an equilibrium emittance beam: (a) the resolution in x, (b) the resolution in y, (c) the resolution in p_x, and (d) the resolution in p_y. In each case, the RMS resolution is recorded in the figure and the ratio of the RMS resolution with the RMS beam spread in the coordinate is recorded as RMS/RMS.

Figure 25 shows the resolution in each of the four transverse-phase-space variables. The precision with which the transverse position-coordinates are measured is significantly below 10% of the RMS spread of the beam. The ratio of the RMS resolution to the RMS beam spread in p_x is 11.5% and in p_y is 8.5%. At 11.5%, the p_x resolution is consistent with the requirement that the bias in the emittance be less than 1% (but only just) and fails (but only just) the specification defined in section 7.4.1.1.

Ten samples of matched beams, each of one million events, were generated with transverse emittances between 0.5 π mm rad and 9.5 π mm rad. G4MICE was used to simulate the passage of the muons through MICE. The transverse emittance was calculated using the reconstructed tracks. Figure 26 shows the emittance resolution obtained analysing the equilibrium emittance (2.5 π mm rad) sample. The one million events in the sample were split into 20 sub-samples of 50,000 events; the emittance was calculated for each sub-sample. The bias in the upstream tracker is -0.12%; that in the downstream tracker is 1.6%. The RMS spread of the distributions is 0.65% for the upstream tracker and 1.9% for the downstream tracker.

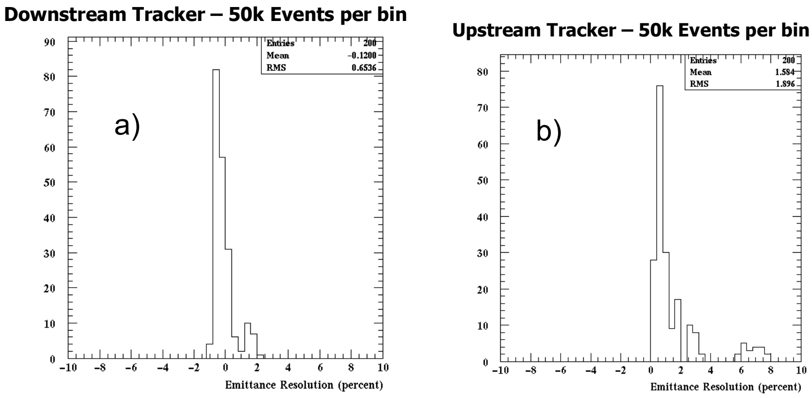

Figure 26: Resolution in uncorrected emittance for the measurement of the emittance in the upstream tracker (a) and the downstream tracker (b). The plots were made for the ten matched beams described in the text. The resolution is plotted relative to the generated emittance and expressed as a percentage. One entry in each histogram corresponds to the emittance calculated from one 50,000 event sub-sample.

The various matrices required by the correction procedure were obtained using one of the 50,000 event sub-samples. Figure 27 shows the distributions of corrected emittance in both the upstream and the downstream trackers using the same 20 sub-samples of 50,000 events at equilibrium emittance. The bias in the reconstructed emittance has been removed and the RMS resolution in the upstream tracker is 0.14% while that in the downstream tracker is 0.20%.

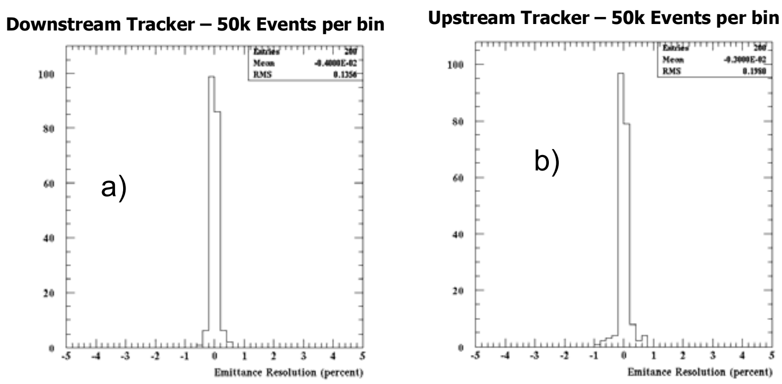

Figure 27: Resolution in corrected emittance for the measurement of the emittance in the upstream tracker (a) and the downstream tracker (b). The plots were made for the ten matched beams described in the text. The resolution is plotted relative to the generated emittance and expressed as a percentage. One entry in each histogram corresponds to the emittance calculated from one 50,000 event sub-sample.

A similar analysis was performed for each of the ten samples. Figure 28a compares the change in emittance obtained using the true parameters of the muon tracks with that obtained using the reconstructed parameters. In each case, the reconstructed emittance reproduces the true value. Note that scraping of the high-emittance beams causes the sample of muons transported down the channel to have an emittance smaller than that generated.

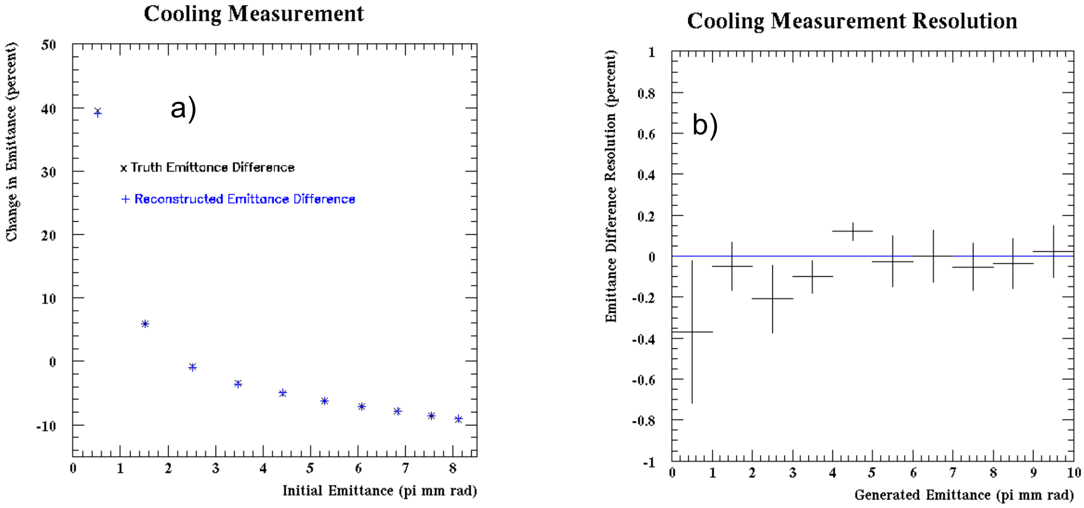

Figure 28: a) Relative change in emittance between the upstream and the downstream trackers as a function of the generated emittance at the upstream tracker. The emittance reconstructed using the generated muon parameters are shown as the black stars while the blue crosses show the reconstructed emittance. b) Resolution in the relative change in emittance plotted as a function of the generated emittance at the upstream tracker.

7.4.2.2 Two-dimensional, longitudinal, emittance

At present, a simulation of the beam distributions in energy and time is not available. To make an estimate of the performance of the tracking system in the measurement of longitudinal emittance, therefore, the matched equilibrium-emittance sample (2.5 π mm rad) beam used in the transverse-emittance performance-analysis was used and Gaussian distributions in time and energy generated. The spread of the beam in time and energy was taken from the beam arriving at the cooling channel in Study II [3]. The standard deviation of the time distribution was taken to be 510 ps and that of the kinetic-energy distribution 25 MeV. Since, by construction, the beam contains no correlation between the transverse and longitudinal parameters, the six-dimensional emittance factorises into the transverse emittance multiplied by the longitudinal emittance. The analysis presented in this section, therefore, concentrates on the reconstruction of the longitudinal emittance. The full tracker-simulation was used to evaluate the muon energy. The resolution of the time measurement was simulated using a Gaussian distribution with a standard deviation of 50 ps. It was assumed that this resolution was available at the upstream tracker. The time resolution assumed therefore corresponds to a best case since the time-of-flight system specification calls for a resolution of 70 ps per plane which corresponds to 50 ps per time-of-flight hodoscope. The effect of the time resolution on the bias and resolution of the reconstructed emittance is investigated below.

The normalised longitudinal emittance, ε_{2N}, is defined by [3]

$$\varepsilon_{2N} = \frac{1}{m_\mu}\sqrt[2]{|V_2|}$$

where V_2 is the covariance matrix of the time and energy (t, E) distributions of the muon beam. To assess the degree to which the tracker meets the specification, the measured RMS resolution values of each of the phase-space coordinates t, E must be compared to the RMS spread of the same variable in the beam described above.

Figure 29 shows the resolution of the momentum component parallel to the beam axis, p_z, and E. The ratio of the RMS resolution in p_z and E to the RMS spread of the beam is 16% in the case of p_z and 14% for E. Again, the resolution achieved is somewhat in excess of the 10% figure of merit defined in section 7.4.1.1.

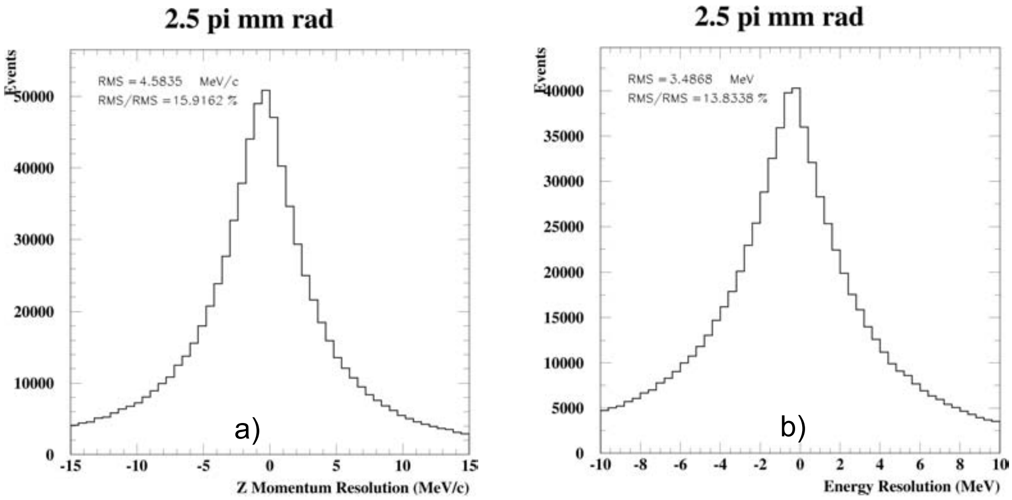

Figure 29: Resolution in longitudinal phase-space coordinates reconstructed using the beam described in the text: (a) the resolution in p_z, and (b) the resolution in E. In each case, the RMS resolution is recorded in the figure and the ratio of the RMS resolution with the RMS beam spread in the coordinate is recorded as RMS/RMS.

The one million events in the event sample were again split up into 20 sub-samples each of 50,000 events and the longitudinal emittance calculated for each sub-sample. Figure 30 shows the longitudinal-emittance resolution for both the upstream and the downstream tracker. The bias in the upstream tracker is 3.6%; that in the downstream tracker is 4.2%. The RMS spread of the distribution is 0.16% for the upstream tracker and 0.12% for the downstream.

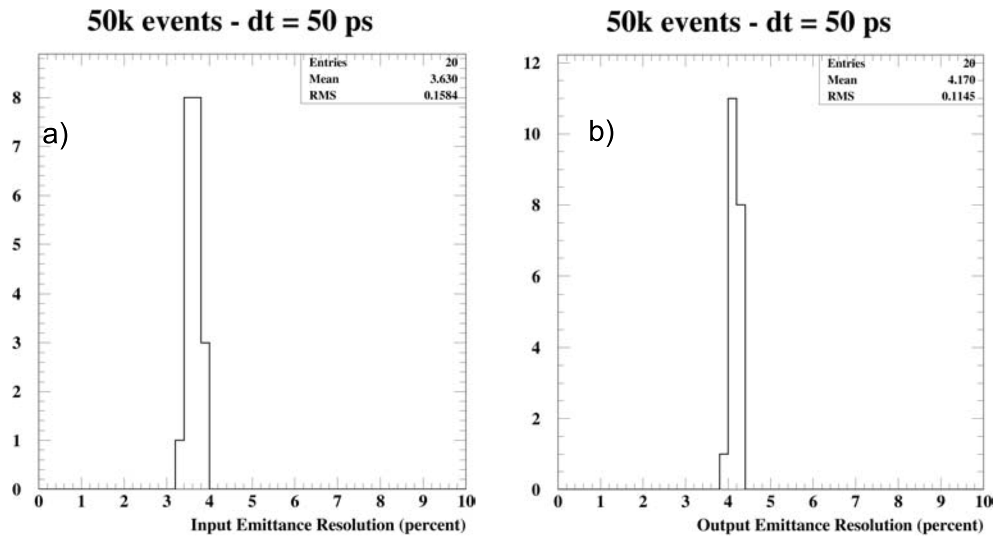

Figure 30: Resolution in measured uncorrected longitudinal emittance in the upstream tracker (a) and the downstream tracker (b). The plots were made using the beam described in the text. The resolution is plotted relative to the generated emittance and expressed as a percentage. One entry in each histogram corresponds to the emittance calculated from one 50,000 event sub-sample.

Once again, the various correction matrices defined in section 7.4.1.2 were calculated using one of the 50,000 event sub-samples and used to correct each of the 20 sub-samples. Figure 31 shows the distributions of corrected emittance in the upstream and downstream trackers. The bias in the reconstructed emittance has been removed and the RMS resolution in the upstream tracker is 0.16% while that in the downstream tracker is 0.12%.

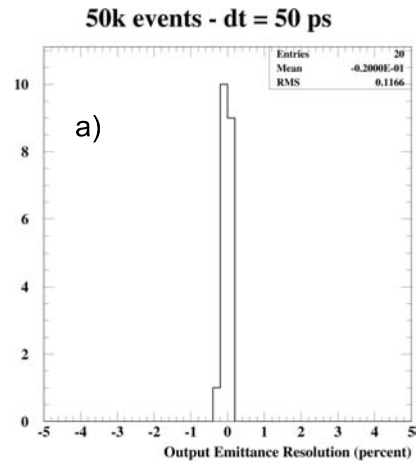

Figure 31: Resolution in measured corrected longitudinal emittance in the upstream tracker (a) and the downstream tracker (b). The plots were made using the beam described in the text. The resolution is plotted relative to the generated emittance and expressed as a percentage. One entry in each histogram corresponds to the emittance calculated from one 50,000 event sub-sample.

Section 7.4.1.1 showed how the bias in the reconstructed emittance is related to the ratio of the RMS resolution divided by the RMS spread of the beam distribution. The bias in the uncorrected emittance is plotted in figure 32a as a function of the uncertainty in the time measurement and in figure 32b as a function of the uncertainty in the energy measurement. The time measurement uncertainty was varied by modifying the standard deviation of the Gaussian distribution used to smear the time measured in the time-of-flight system while using the track-reconstruction code to determine the energy. To vary the energy resolution, the true energy of the muon was smeared using a Gaussian distribution while keeping the time resolution fixed at 50 ps.

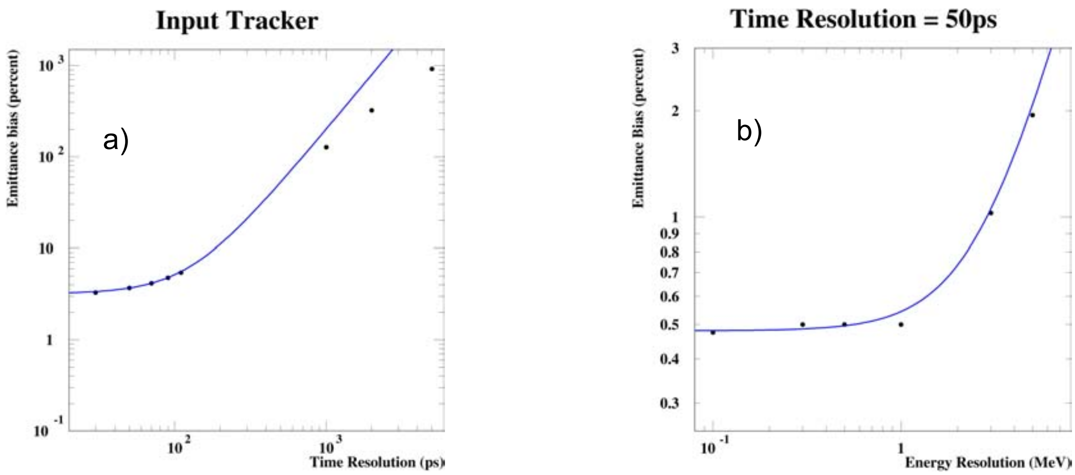

Figure 32: Longitudinal-emittance bias as a function of the time resolution (a) and energy resolution (b) assumed in the simulation. The points represent the results of the simulation described in the text. The solid line shows the result of the simple calculation of the bias as a function of the RMS resolution described in section 7.4.1.1.

8. Safety and integration

Since the fibre tracker itself is a totally passive device and its impact on the safe operation of MICE is minimal. With the exception of the Hall probes required to monitor the stability of the magnetic field, there are no active components in the tracking volume. The only safety issue regards vacuum. Since the tracking volume will be evacuated in order to reduce material presented to the muon beam, the optical feed-throughs and the optical patch panel itself must be rated for pressure. A prototype patch panel will be fabricated and tested for vacuum integrity and stability under pressure in order that the design may be certified. At this point we do not plan to test the final assemblies at pressure.

The fibre tracker readout system only requires standard line voltage (approximately 2 kW per cryostat). The cryogenic system will be based on a closed-cycle refrigerator (a cryocooler) and therefore presents no cryogen or oxygen deficiency hazard.

9. Cost and schedule

The MICE scintillating-fibre tracker cost and schedule analysis is recorded in detail in the MICE Work Breakdown Structure (WBS). The summary information presented here is extracted from the tracker WBS issued on the 14th July 2004. Table 4 shows the capital cost (‘Fixed cost’) of the top-level tasks as well as the cost (‘Cost’) including manpower that must be accounted against the MICE project. The regional contributions to the fixed cost are based on the presently agreed distribution of responsibilities among the MICE collaborating institutes contributing the scintillating-fibre tracker effort. Note that the US manpower cost is understood to be contained within the fixed cost. The Japanese manpower cost is understood not required to be explicitly entered in the MICE WBS and is therefore omitted. In the UK the manpower resources are required to be accounted for explicitly and appear as the difference between the ‘Cost’ and the ‘Fixed cost’. The cost of purchasing new VLPCs and producing a system for MICE is included in the WBS. The tracker group hopes to negotiate the loan of sufficient VLPC cassettes to readout the MICE tracker. Should this loan be successful, the capital cost of the tracker would be reduced by approximately $1M and the loan of the VLPCs would be a significant additional US contribution in kind.

The schedule for the MICE scintillating-fibre tracker, extracted from the 14th July 2004 issue of the tracker WBS, is shown in figure 33. The figure shows the estimated duration of the top-level tasks and the project milestones. The analysis of the data from the first prototype is now complete. The tracker group is presently building a fourth station using techniques that are believed to be those that will be used to build the final tracker modules. In addition, a cryostat cooled using a closed-cycle cryocooler is being manufactured. An assembly will be made that will link the three stations of the first prototype with the fourth station; the resulting four-station tracker will constitute the second MICE prototype tracker. It is planned to expose the second prototype to a test beam in KEK in the summer of 2005. The DØ collaboration has agreed the loan of two VLPC cassettes to allow the second prototype to be readout in the KEK test beam.

Name	Fixed cost	Cost	Fixed cost (Japan)	Fixed cost (UK)	Fixed cost (US)
MICE SiFi	£1424248	£2,198,214.88	¥4.914956E+07	£369193.3	$1466500
First prototype	£42295.2	£42,295.22	¥2407060	£27334.7	$5000
Second prototype and KEK test beam 2005	£94090.45	£94,090.47	¥1.116547E+07	£23988.98	$24500
Full scintillating-fibre tracker	£1287862	£1,419,199.02	¥3.557703E+07	£317869.6	$1437000
Optical connectors	£30279.12	£30,279.12	¥0	£30279.12	$0
Doublet layers	£135074.9	£135,074.91	¥9623344	£57689.1	$52000
Station support	£68500	£158,992.24	¥0	£68500	$0
VLPC System	£980496.6	£980,496.60	¥1.895425E+07	£123401.4	$1385000
Mechanical design (review)	£7000	£7,000.00	¥0	£7000	$0
Assembly and test of tracker	£31000	£71,844.48	¥0	£31000	$0
Tracker DAQ software	£0	£0.00	¥0	£0	$0
UK manpower not explicitly listed against tasks	£0	£642,630.17	¥0	£0	$0
Extracted from the scintillating-fibre section of the MICE WBS (issue of 14 July 2004)					

Table 4: Cost of the MICE scintillating-fibre tracker extracted from the MICE Work Breakdown Structure (issue of 14 July 2004). Details of the assumptions under which the cost information has been derived are described in the text.

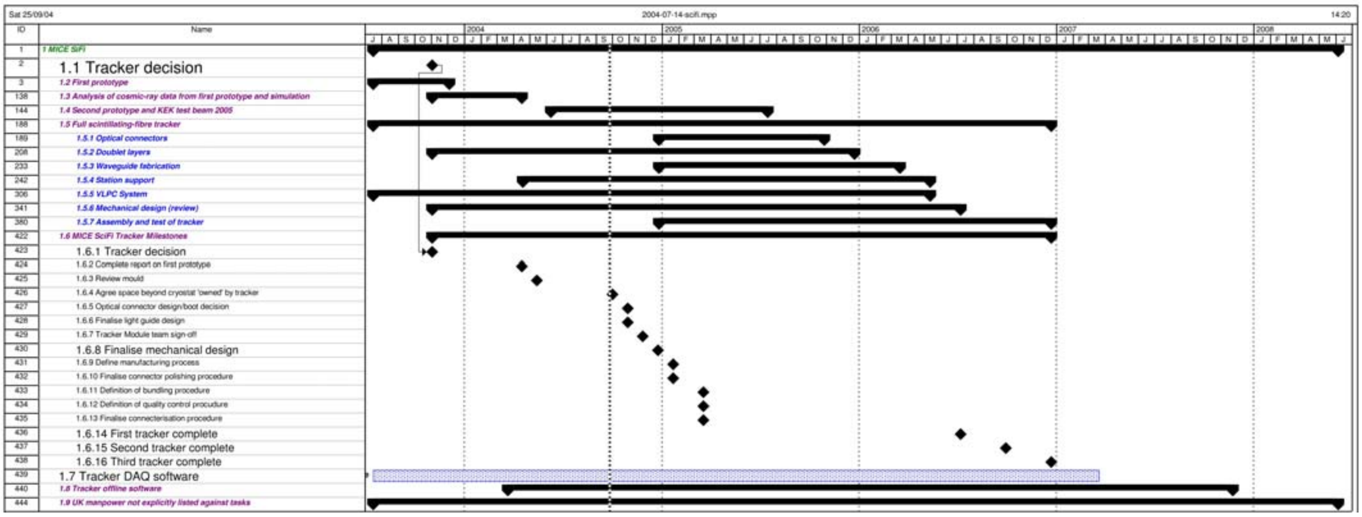

Figure 33: Schedule of the MICE scintillating fibre tracker extracted from the MICE Work Breakdown Structure (issue of 14 July 2004).

Acknowledgements

We would like to thank the DØ department at Fermilab for all their help with the VLPC test stand and with the ribbon fabrication. In particular we wish to thank Bob Kabinsky and Rolando Flores for their help with the production of the scintillating fibre ribbons.

Bibliography

1. S.Geer, Phys. Rev. D **57** (1998) 6989;
   D.Finley, N.Holtkamp, eds, “Feasibility Study on a Neutrino Source Based on a Muon Storage Ring”, (2000). See http://www.fnal.gov/projects/muon_collider/reports.html;
   S. Ozaki, R. Palmer, M. Zisman, and J. Gallardo, eds, “Feasibility Study-II of a Muon-Based Neutrino Source”, BNL-52623, June 2001;
   The Muon Collaboration, Study 2a, http://www.cap.bnl.gov/mumu/study2a/;
   See http://www.cap.bnl.gov/mumu/studyii/FS2-report.html;
   Japanese Neutrino Factory scheme: see http://www-prism.kek.jp/nufactj/nufactj.pdf
   A. Blondel, ed, “ECFA/CERN studies of a European neutrino factory complex”, CERN-2004-022, http://preprints.cern.ch/cernrep/2004/2004-002/2004-002.html.
2. The MICE Collaboration, “An international Muon Ionisation Cooling Experiment (MICE)”, http://mice.iit.edu/mnp/MICE0021.pdf.

3. The MICE Collaboration, “MICE Technical Reference Document - Draft Version”, http://www.isis.rl.ac.uk/accelerator/mice/TR/MICE_Tech_Ref.html.
4. D. Summers and G. Gregoire, ‘Tracker choice: ground rules and process’, MICE Note 52.
5. M.G. Stapelbroek and D. Petroff, in "Proceedings of the Workshop on Scintillating Fiber Detectors, SCIFI 93", University of Notre Dame, 24-28 October, 1993, edited by Bross, Ruchti, and Wayne (World Scientific, Singapore, 1994), p. 621.
6. ‘System tests of the new electronics for the DØ Central Fiber Tracker and Preshower detectors’, J. Estrada et. al., August, 2003, DØ Note 4233.
7. A; T. LeCompte and H.T. Diehl, Ann. Rev. Nucl. Part. Sci. 50, 71 (2000).
8. V. Buscher et al., ‘DØ Testing and characterization of VLPC cassettes’, DØ Note 3912 (2001).
9. L. Babukhadia, ‘The DØ Detector for Run II’, invited talk at the 31st International Conference on High Energy Physics, Amsterdam, the Netherlands, July 24-31, 2002, hep-ex/0210002, Fermilab-Conf-02/239-E
10. B. Baumbaugh et al, ‘Performance of a large scale scintillating fiber tracker using VLPC readout," IEEE Trans. Nucl. Sci. 43, 1146 (1996).
11. SCIFI 97, ‘Conference on Scintillating and Fibe Detectors’, University of Notre Dame, November 1997, edited by Bross, Ruchti, and Wayne, World Scientific, Singapore, 1998.
12. M. Utes, ‘SVX2E ASIC testing results’, September 1996, DØ Note 3095.
13. A. Lobodenko, ‘MIL 1553B control and monitor’, DØ Note 3886, July 2001.
14. Jones, Kephart, and Vidal, ‘Tevatron bunch length studies at CDF’, FERMILAB-TM-2172, May 2002.
15. Oriel UV-Visible silicon diode photodetector model 70331, Oriel Instruments, Stratford, CT, USA.
16. J.J. Gomez Cadenas, J.A. Hernando Morata, A. Cervera Villanueva, ‘"RecPack", a general reconstruction tool-kit’, poster presented at Computing in High Energy Physics 2004, Interlaken, Switzerland 27th September - 1st October 2004; http://indico.cern.ch/contributionDisplay.py?contribId=269&sessionId=24&confId=0

17 T. Roberts, K. Tilley, ‘Beam line design and optimisation: update’, talk presented at the MICE video conference, 14th July 2004, http://hep04.phys.iit.edu/cooldemo/vc/vc63/vc63_roberts_beamline.ppt

18. Documentation on the MICE software suite is to be found at: http://hep04.phys.iit.edu/cooldemo/software/software.html;
for documentation on G4MICE see http://hep04.phys.iit.edu/cooldemo/software/micegeant4.html;
G4BeamLine documentation: T. Robers, http://www.muonsinc.com/g4beamline.html.
Documentation on Geant4 is to be found at http://wwwasd.web.cern.ch/wwwasd/geant4/geant4.html.
19. K.L. Brown, Ch. Iselin, D.C. Carey: Decay Turtle, CERN 74-2 (1974);
U. Rohrer: Compendium of Decay Turtle Enhancements;
C. Kost, P. Reeve: REVMOC - A Monte Carlo Beam Transport Program, TRI-DN-82-28 (1983);
see also http://pc532.psi.ch/turtle.htm.
20. R. Sandstrom, ‘RF background simulation: proposal for baseline’, talk presented at the MICE Collaboration Video Conference on the 22nd September 2004, http://hep04.phys.iit.edu/cooldemo/vc/vc66/vc66_sandstrom_rfbackground.ppt.
21. A. Blondel, P. Janot, ‘Spectrometer design’, talk presented at the MUCOOL and MICE Collaboration meeting, Illinois Institute of Technology February 5 - 8, 2002 http://agni.phys.iit.edu/~capp/workshops/mumice02/talks/Blondel_spectrodesign.ppt

22. C. Rogers contribution to 'Tracker update: performance', talk presented by M. Ellis at the MICE Collaboration Video Conference on the 13th January 2005; http://hep04.phys.iit.edu/cooldemo/vc/vc72/vc72_ellis_tracker.ppt.